

# Measurement of the CMB temperature power spectrum and constraints on cosmology from the SPT-3G 2018 TT,TE, and EE dataset

L. Balkenhol<sup>1,\*</sup>, D. Dutcher<sup>2</sup>, A. Spurio Mancini<sup>3</sup>, A. Doussot<sup>4</sup>, K. Benabed<sup>4</sup>, S. Galli<sup>4</sup>, P. A. R. Ade<sup>5</sup>, A. J. Anderson<sup>6,7,8</sup>, B. Ansarinejad<sup>1</sup>, M. Archipley<sup>9,10</sup>, A. N. Bender<sup>11,7,8</sup>, B. A. Benson<sup>6,7,8</sup>, F. Bianchini<sup>10</sup>,<sup>12,13,14</sup>, L. E. Bleem<sup>11,7</sup>, F. R. Bouchet<sup>14</sup>, L. Bryant<sup>15</sup>, E. Camphuis<sup>4</sup>, J. E. Carlstrom<sup>7,15,16,11,8</sup>, T. W. Cecil<sup>11</sup>, C. L. Chang<sup>11,7,8</sup>, P. Chaubal<sup>16</sup>, P. M. Chichura<sup>16,7</sup>, T.-L. Chou<sup>16,7</sup>, A. Coerver<sup>17</sup>, T. M. Crawford<sup>7,8</sup>, A. Cukierman<sup>12,14,13,18</sup>, C. Daley<sup>9</sup>, T. de Haan<sup>9</sup>, K. R. Dibert<sup>8,7</sup>, M. A. Dobbs<sup>20,21</sup>, W. Everett<sup>22</sup>, C. Feng<sup>23</sup>, K. R. Ferguson<sup>24</sup>, A. Foster<sup>25</sup>, A. E. Gambreł<sup>26,27</sup>, R. W. Gardner<sup>15</sup>, N. Goeckner-Wald<sup>13,12</sup>, R. Gualtieri<sup>11</sup>, F. Guidi<sup>10</sup>, S. Guns<sup>17</sup>, N. W. Halverson<sup>26,27</sup>, E. Hivon<sup>10</sup>, G. P. Holzapfel<sup>23</sup>, W. L. Holzapfel<sup>17</sup>, J. C. Hood<sup>7</sup>, N. Huang<sup>17</sup>, L. Knox<sup>28</sup>, M. Korman<sup>25</sup>, C.-L. Kuo<sup>12,13,14</sup>, A. T. Lee<sup>17,29</sup>, A. E. Lowitz<sup>7,30</sup>, C. Lu<sup>23</sup>, M. Millea<sup>17</sup>, J. Montgomery<sup>20</sup>, Y. Nakato<sup>13</sup>, T. Natoli<sup>7,8</sup>, G. I. Noble<sup>31,32</sup>, V. Novosad<sup>33</sup>, Y. Omori<sup>8,7</sup>, S. Padin<sup>7,18</sup>, Z. Pan<sup>11,7,16</sup>, P. Paschos<sup>15</sup>, K. Prabhu<sup>28</sup>, W. Quan<sup>16,7</sup>, M. Rahimi<sup>1</sup>, A. Rahlin<sup>6,7</sup>, C. L. Reichardt<sup>1</sup>, M. Rouble<sup>20</sup>, J. E. Ruhl<sup>25</sup>, E. Schiappucci<sup>1</sup>, G. Smecher<sup>34</sup>, J. A. Sobrin<sup>6,7</sup>, A. A. Stark<sup>35</sup>, J. Stephen<sup>15</sup>, A. Suzuki<sup>29</sup>, C. Tandoi<sup>9</sup>, K. L. Thompson<sup>12,13,14</sup>, B. Thorne<sup>28</sup>, C. Tucker<sup>5</sup>, C. Umlitla<sup>10</sup>, J. D. Vieira<sup>9,23,10</sup>, G. Wang<sup>11</sup>, N. Whitehorn<sup>36</sup>, W. L. K. Wu<sup>10</sup>, M. R. Young<sup>6,7</sup>, and J. A. Zebrowski<sup>7,8,6,17</sup>

(SPT-3G Collaboration)

<sup>1</sup>School of Physics, University of Melbourne, Parkville VIC 3010, Australia

<sup>2</sup>Joseph Henry Laboratories of Physics, Jadwin Hall, Princeton University, Princeton, New Jersey 08544 USA

<sup>3</sup>Mullard Space Science Laboratory, University College London, Holmbury St. Mary, Dorking, Surrey RH5 6NT, United Kingdom

<sup>4</sup>Sorbonne Université, CNRS, UMR 7095, Institut d’Astrophysique de Paris, 98 bis bd Arago, 75014 Paris, France

<sup>5</sup>School of Physics and Astronomy, Cardiff University, Cardiff CF24 3YB, United Kingdom

<sup>6</sup>Fermi National Accelerator Laboratory, MS209, P.O. Box 500, Batavia, Illinois 60510, USA

<sup>7</sup>Kavli Institute for Cosmological Physics, University of Chicago, 5640 South Ellis Avenue, Chicago, Illinois 60637, USA

<sup>8</sup>Department of Astronomy and Astrophysics, University of Chicago, 5640 South Ellis Avenue, Chicago, Illinois 60637, USA

<sup>9</sup>Department of Astronomy, University of Illinois Urbana-Champaign, 1002 West Green Street, Urbana, Illinois 61801, USA

<sup>10</sup>Center for Astrophysics & Surveys, National Center for Supercomputing Applications, Urbana, Illinois 61801, USA

<sup>11</sup>High-Energy Physics Division, Argonne National Laboratory, 9700 South Cass Avenue, Lemont, Illinois 60439, USA

<sup>12</sup>Kavli Institute for Particle Astrophysics and Cosmology, Stanford University, 452 Lomita Mall, Stanford, California 94305, USA

<sup>13</sup>Department of Physics, Stanford University, 382 Via Pueblo Mall, Stanford, California 94305, USA

<sup>14</sup>SLAC National Accelerator Laboratory, 2575 Sand Hill Road, Menlo Park, California 94025, USA

<sup>15</sup>Enrico Fermi Institute, University of Chicago, 5640 South Ellis Avenue, Chicago, Illinois 60637, USA

<sup>16</sup>Department of Physics, University of Chicago, 5640 South Ellis Avenue, Chicago, Illinois 60637, USA

<sup>17</sup>Department of Physics, University of California, Berkeley, California 94720, USA

<sup>18</sup>California Institute of Technology, 1200 East California Boulevard, Pasadena, California 91125, USA

<sup>19</sup>High Energy Accelerator Research Organization (KEK), Tsukuba, Ibaraki 305-0801, Japan

<sup>20</sup>Department of Physics and McGill Space Institute, McGill University, 3600 Rue University, Montreal, Quebec H3A 2T8, Canada

<sup>21</sup>Canadian Institute for Advanced Research, CIFAR Program in Gravity and the Extreme Universe, Toronto, Ontario M5G 1Z8, Canada

<sup>22</sup>Department of Astrophysical and Planetary Sciences, University of Colorado, Boulder, Colorado 80309, USA

<sup>23</sup>Department of Physics, University of Illinois Urbana-Champaign, 1110 West Green Street, Urbana, Illinois 61801, USA

<sup>24</sup>Department of Physics and Astronomy, University of California, Los Angeles, California 90095, USA

<sup>25</sup>Department of Physics, Case Western Reserve University, Cleveland, Ohio 44106, USA

<sup>26</sup>CASA, Department of Astrophysical and Planetary Sciences, University of Colorado, Boulder, Colorado 80309, USA

<sup>27</sup>Department of Physics, University of Colorado, Boulder, Colorado 80309, USA

<sup>28</sup>Department of Physics and Astronomy, University of California, One Shields Avenue, Davis, California 95616, USA

<sup>29</sup>Physics Division, Lawrence Berkeley National Laboratory, Berkeley, California 94720, USA

<sup>30</sup>Steward Observatory and Department of Astronomy, University of Arizona, 933 N. Cherry Avenue, Tucson, Arizona 85721, USA

<sup>31</sup>Dunlap Institute for Astronomy and Astrophysics, University of Toronto, 50 St. George Street, Toronto, Ontario M5S 3H4, Canada

<sup>32</sup>David A. Dunlap Department of Astronomy and Astrophysics, University of Toronto, 50 St. George Street, Toronto, Ontario M5S 3H4, Canada

<sup>33</sup>Materials Sciences Division, Argonne National Laboratory, 9700 South Cass Avenue, Lemont, Illinois 60439, USA

<sup>34</sup>Three-Speed Logistic, Victoria, British Columbia V8S 3Z5, Canada

<sup>35</sup>Harvard-Smithsonian Center for Astrophysics, 60 Garden Street, Cambridge, Massachusetts 02138, USA

<sup>36</sup>Department of Physics and Astronomy, Michigan State University, East Lansing, Michigan 48824, USA



(Received 11 December 2022; accepted 7 June 2023; published 13 July 2023)

We present a sample-variance-limited measurement of the temperature power spectrum (TT) of the cosmic microwave background using observations of a  $\sim 1500^2$  field made by the SPT-3G in 2018. We report multifrequency power spectrum measurements at 95, 150, and 220 GHz covering the angular multipole range  $750 \leq l < 3000$ . We combine this TT measurement with the published polarization power spectrum measurements from the 2018 observing season and update their associated covariance matrix to complete the SPT-3G 2018 TT=TE=EE dataset. This is the first analysis to present cosmological constraints from SPT TT, TE, and EE power spectrum measurements jointly. We blind the cosmological results and subject the dataset to a series of consistency tests at the power spectrum and parameter level. We find excellent agreement between frequencies and spectrum types and our results are robust to the modeling of astrophysical foregrounds. We report results for  $\Lambda$ CDM and a series of extensions, drawing on the following parameters: the amplitude of the gravitational lensing effect on primary power spectra  $A_L$ , the effective number of neutrino species  $N_{\text{eff}}$ , the primordial helium abundance  $Y_P$ , and the baryon clumping factor due to primordial magnetic fields  $b$ . We find that the SPT-3G 2018 TT=TE=EE data are well fit by  $\Lambda$ CDM with a probability to exceed of 15%. For  $\Lambda$ CDM, we constrain the expansion rate today to  $H_0 = 68.3 \pm 1.5 \text{ km s}^{-1} \text{ Mpc}^{-1}$  and the combined structure growth parameter to  $S_8 = 0.797 \pm 0.042$ . The SPT-based results are effectively independent of Planck, and the cosmological parameter constraints from either dataset are within  $< 1\sigma$  of each other. The addition of temperature data to the SPT-3G TE=EE power spectra improves constraints by 8–27% for each of the  $\Lambda$ CDM cosmological parameters. When additionally fitting  $A_L$ ,  $N_{\text{eff}}$ , or  $N_{\text{eff}} \pm Y_P$ , the posteriors of these parameters tighten by 5–24%. In the case of primordial magnetic fields, complete TT=TE=EE power spectrum measurements are necessary to break the degeneracy between  $b$  and the spectral index of primordial density perturbations. We report a 95% confidence upper limit from SPT-3G data of  $b < 1.0$ . The cosmological constraints in this work are the tightest from SPT primary power spectrum measurements to date and the analysis forms a new framework for future SPT analyses.

DOI: [10.1103/PhysRevD.108.023510](https://doi.org/10.1103/PhysRevD.108.023510)

## I. INTRODUCTION

The temperature and polarization anisotropies imprinted in the cosmic microwave background (CMB) during recombination encode information on the contents and dynamics of the early Universe. High-precision

measurements of the CMB power spectra by satellites and ground-based telescopes enable us to determine the six free parameters of the standard  $\Lambda$  cold dark matter ( $\Lambda$ CDM) model with exceptional precision and place tight limits on possible model extensions [1–5]. Improving measurements of the CMB anisotropies is a key science goal of ground-based CMB experiments such as the South Pole Telescope (SPT hereafter) [6], the Atacama Cosmology Telescope (ACT hereafter) [7], POLARBEAR [8], and BICEP/Keck [9, 10].

\* Corresponding author.  
lbalkenhol@student.unimelb.edu.au

The Planck satellite has mapped the CMB temperature  $\sim 1500$  deg $^2$  in the southern sky divided into four subfields. anisotropies down to scales of approximately seven arcminutes to the cosmic-variance limit [11] and contemporary interest is shifting to polarization data; precision measurements of small angular scale modes of the TE and EE spectra have significant cosmological constraining power [12]. Nevertheless, the TT power spectrum is two orders of magnitude larger than the polarization spectra and temperature data dominate the constraining power of seminal CMB datasets [11, 13–16]. Complete TT=TE=EE datasets have significantly more constraining power in  $\Lambda$ CDM compared to TE=EE data alone, based simply on a mode-counting argument. Moreover, certain extensions to the standard model, e.g. primordial magnetic fields, can only be effectively constrained by full TT=TE=EE data [17] due to parameter degeneracies.

In this work, we present cosmological constraints from TT=TE=EE power spectrum measurements obtained from observations of an approximately 1500 deg $^2$  region in the southern sky made by SPT-3G [18], the latest receiver installed on the SPT, in 2018. The complete SPT-3G 2018 TT=TE=EE dataset comprises previously unpublished TT data, which we present here, and the polarization power spectra presented by Dutcher et al. [2] with an updated covariance matrix. We present cosmological constraints on  $\Lambda$ CDM and a series of extensions, drawing on the following parameters: the amplitude of the gravitational lensing effect on primary power spectra, the effective number of neutrino species  $N$ , the primordial helium abundance  $Y$ , and the baryon clumping factor due to primordial magnetic fields  $b$ . We describe our blinding procedure and present in-depth assessment of the consistency between frequencies and spectrum types.

This paper is structured as follows. In Sec. II we summarize important aspects of the data and analysis pipeline of D21 and highlight key changes we make. In Sec. III we present the updated likelihood code including the foreground model used for temperature data and details of the parameter fitting procedure. We demonstrate the consistency of the SPT-3G 2018 data in Sec. IV and show the TT=TE=EE power spectra in Sec. V. We report cosmological constraints in Sec. VI and summarize our findings in Sec. VII.

## II. DATA AND ANALYSIS

Sobrin et al. [19] present the SPT-3G instrument and detail the 2018 observations and describe the associated processing pipeline. These aspects of the analysis have changed. We briefly summarize key aspects here and refer the reader to D21 and Sobrin et al. [19] for complete discussions.

The data presented here were collected by SPT-3G during an observation period of four months in 2018. The main SPT-3G survey field covers an area of

We calibrate the time-ordered data (TOD) using a series of calibration observations of galactic HII regions. Sources brighter than 50 mJy at 150 GHz are masked and we filter the TOD using low- and high-pass filters, as well as a common-mode filter. The filtered TOD are processed into maps with  $2^0$  square pixels using the Lambert azimuthal equal-area projection. We form a set of  $N \approx 30$  temperature and polarization maps with approximately uniform noise properties, so-called “bundles.” We calculate cross-spectra between these bundles and bin them into “band powers.” We debias the band powers following the MASTER framework [20] using a suite of simulations, thereby accounting for the effects of the survey mask, the TOD filtering, as well as the instrument beam and the pixel window function. Lastly, we derive absolute per-subfield and full-field calibrations through comparison with Planck data [11].

The analysis in D21 is designed to maximize sensitivity to the polarization spectra on intermediate and small angular scales. The common-mode filter applied to the TOD heavily suppresses temperature anisotropies on scales larger than a quarter of a degree. We therefore set a minimum angular multipole for TT spectra of  $TT_{\min} \approx 750$ .

We make two updates to the calculation of the band power covariance matrix. First, we account for correlated noise between frequencies in intensity. For  $l < 1000$ , the atmospheric noise in the 150 and 220 GHz data are highly correlated. Because the noise in the 220 GHz data is an order of magnitude larger compared to the 150 GHz data, the former data require precision modeling of the noise correlation. For this reason, we exclude the  $150 \times 220$  GHz and  $220 \times 220$  GHz spectra at  $l < 1000$ . Second, we improve the treatment of bin-to-bin correlations induced by the flat-sky projection step. We detail changes to the covariance matrix and their impact on the results reported in D21 in Appendix A.

### A. Blinding

In a key change from D21 and past SPT TT, TE, and EE analysis, we blind parameter constraints until a series of consistency tests are passed, which we detail in Sec. IV. Our blinding procedure entails offsetting cosmological results by random vectors prior to plotting parameter constraints and removing axes labels where appropriate. We blind parameter constraints until the following consistency tests are passed: (1) null tests, (2) comparison of a minimum-variance combination of band powers to the full multifrequency data vector, (3) conditional spectrum tests split by frequency, (4) conditional spectrum tests split by spectrum type assuming  $\Lambda$ CDM, and (5) comparison of cosmological parameter constraints in  $\Lambda$ CDM between subsets and the full dataset. Note that the last two tests are model dependent; in principle, failures of these tests do not prevent cosmological inference but invite further analysis within the chosen model. In addition to these quantitative preconditions,

test the robustness of our cosmological results under variations of the likelihood and commit to investigating any significant impact on key results.

### III. PARAMETER FITTING, MODELING, AND EXTERNAL DATA

We use the Markov chain Monte Carlo (MCMC) package `COSMOMC` [21]<sup>1</sup> to obtain cosmological parameter constraints. We compute theoretical CMB spectra using `CAMB` [22]<sup>2</sup> and `CosmoPower` [23]<sup>3</sup>. We parametrize the  $\Lambda$ CDM model using the following: the physical density of cold dark matter,  $\Omega_c h^2$ , and baryons,  $\Omega_b h^2$ , the optical depth to reionization  $\tau$ , the amplitude  $A$  and spectral index  $n_s$  of primordial density perturbations (with  $A$  defined at a pivot scale of 0.05 Mpc<sup>1</sup>), and a parameter that approximates the sound horizon at recombination,  $\theta_{MC}$  [24].

When not combining with Planck data, we include a Planck-based Gaussian prior on the optical depth to reionization of  $\tau \approx 0.0540 \pm 0.0074$ . This parameter is primarily constrained by a bump at  $l < 10$  in  $T_E = E_E$ . Omitting this prior leads to a degeneracy between  $\tau$  and  $A$  as the amplitude of the power spectra over the angular multipole range probed by our data depends on  $\tau$  mostly through the combination  $A e^{-2\tau}$ .

Similar to D21, we verify that the likelihood is unbiased using 100 sets of simulated band powers generated using the data covariance matrix. We obtain the best-fit model for each realization using the likelihood code. We find that the average value for each cosmological parameter across the set of simulations lies within  $< 1.5$  standard errors (i.e., the standard deviation of the ensemble divided by  $\sqrt{100}$ ) of the input value. The likelihood code is made publicly available on the SPT website.<sup>4</sup>

#### A. CosmoPower

Spurio Mancini et al. [23] present `CosmoPower`, a neural-network-based CMB power spectrum emulator. Akin to other emulators (e.g. [25]), once trained, `CosmoPower` provides CMB power spectra in a fraction of the time it takes to evaluate Boltzmann solvers such as `CAMB` [22] or `CLASS` [26]. We train `CosmoPower` on a set of power spectra obtained using `CAMB` at high accuracy settings for the  $\Lambda$ CDM,  $\Lambda$ CDM  $\pm N_{eff}$ , and  $\Lambda$ CDM  $\pm A_L$  models.

The constraints obtained by `CosmoPower` (run at default accuracy) are within  $< 0.1\sigma$  of each other for all models. This also highlights that for the analysis of SPT-3G 2018 data, the default accuracy settings used in `CAMB` are sufficient. The trained `CosmoPower` models are made publicly available on the SPT website.

#### B. Foreground model and nuisance parameters

We introduce several foreground and nuisance parameters into our likelihood. We account for the instrumental beam and calibration, aberration due to the relative motion with respect to the CMB rest frame [28], and super-sample lensing [29] in the same way as D21. The polarized foreground model is minorly updated from D21, and we describe it briefly below. Because we include the TT spectrum in this work, we must model the much more complex temperature foregrounds and we describe this modeling in detail below. The baseline priors are summarized in Table VIII in Appendix B.

#### 1. Temperature foregrounds

For the SPT-3G 2018 data with a flux cut for point sources of 50 mJy at 50 GHz, extragalactic foregrounds dominate over the CMB at  $l \geq 2650$ ,  $l \geq 3000$ , and  $\geq 2450$  at 95, 150, and 220 GHz, respectively. We construct a foreground model largely based on the existing likelihoods of Reichardt et al. [30], George et al. [31], and Dunkley et al. [32]. We perform a reanalysis of Reichardt et al. [30] data using the foreground model described below to derive constraints on nuisance parameters. Where appropriate, we account for the different effective band centers of the data and the lower flux cut of Reichardt et al. [30] using the population model of De Zotti et al. [33]. We conservatively widen the constraints from Reichardt et al. [30] data on amplitude parameters and spectral indices by factors of 4 and 2, respectively, before adopting them as priors in the cosmological analysis of SPT-3G data. We perform an analysis of Planck data on the SPT-3G survey patch to set priors on the galactic cirrus contribution.

We model the contribution of the galactic cirrus as a modified blackbody with temperature  $T_d \approx 19.6$  K and spectral index  $\beta_{cirrus}^{cirus}$  with a cross-frequency power spectrum of

$$D_{l;vx\mu}^{cirrus} \approx A_{80}^{cirrus} \frac{g_{\nu}^{\mu} g_{\nu}^{\mu}}{g_{\nu}^{cirrus}^2} \frac{v_{\mu}}{v_{0}^{cirrus} v_{0}^{cirrus}} \frac{\beta_{cirrus}}{80} \frac{l}{\alpha_{cirrus}^2} ;$$

<sup>1</sup><https://cosmologist.info/cosmomc/>.

<sup>2</sup><https://camb.info/>.

<sup>3</sup><https://github.com/alessiospuriomancini/cosmopower/>.

<sup>4</sup><https://pole.uchicago.edu/public/data/balkenhol22/>.

<sup>5</sup>We chose settings similar to the high accuracy settings Hill et al. [27] use to update ACT DR4 results (cf. Appendix A therein); we generate `CAMB` training spectra with

- (i) `k_eta_max` = 144000,
- (ii) `AccuracyBoost` = 2.0,
- (iii) `ISampleBoost` = 2.0,
- (iv) `IAccuracyBoost` = 2.0.

where  $\nu_0 \approx 150$  GHz is the reference frequency,  $\alpha_{cirrus}^{cirus}$  is the amplitude parameter,  $\beta_{cirrus}^{cirus}$  the power law index, and

<sup>6</sup><https://pole.uchicago.edu/public/data/balkenhol22/>.

$g \frac{1}{4} B_v \delta T_d \delta \partial B_v \delta T \delta B_v = \delta T \delta j_{\text{CMB}}$  with the Planck function  $B_v \delta T$  and CMB temperature taken from Fixsen [34]. The spectral index, amplitude parameter, and power law index are free parameters in this model.

We account for Poisson-distributed unresolved radio galaxies and dusty star-forming galaxies with a combined contribution to each cross-frequency spectrum of

$$D_{l;v \times \mu}^{\text{TT;Poisson}} \frac{1}{4} D_{3000;v \times \mu}^{\text{TT;Poisson}} \frac{l^2}{3000}; \quad \delta 2p$$

where we vary the six amplitude parameters  $D_{3000;v \times \mu}^{\text{TT;Poisson}}$  in the likelihood.

Following George et al. [31] and Dunkley et al. [32], we model the clustering term of the cosmic infrared background (CIB) using a modified blackbody spectrum at 25 K with spectral index  $\beta^{\text{CIB-cl}}$ .<sup>7</sup> Like George et al. [31] and Dunkley et al. [32] we use a power law for the angular dependence of this foreground contaminant:

$$D_{l;v \times \mu}^{\text{CIB-cl}} \frac{1}{4} A_{80}^{\text{CIB-cl}} \frac{g \delta v \delta g \mu \delta \beta}{g \delta \delta \delta \delta \delta \delta} \frac{v \mu}{v_0^{\text{CIB-cl}} v_0^{\text{CIB-cl}}} \frac{l^{0.8}}{80}; \quad \delta 3p$$

where the amplitude  $A_{80}^{\text{CIB-cl}}$  and spectral index  $\beta^{\text{CIB-cl}}$  are free parameters,  $v_0^{\text{CIB-cl}} \approx 150$  GHz is the reference frequency, and the value of the power-law index is motivated by Addison et al. [35].

Following Reichardt et al. [30], we account for the thermal Sunyaev-Zeldovich (TSZ) effect by rescaling the power spectrum of Shaw et al. [36] normalized at  $l \approx 3000$ ,  $D_l^{\text{TSZ;template}}$ , at a reference frequency of  $v_0^{\text{TSZ}} \approx 143$  GHz via

$$D_{l;v \times \mu}^{\text{TSZ}} \frac{1}{4} A^{\text{TSZ}} \frac{f \delta v \delta f \delta \mu \delta \beta}{f \delta v_0^{\text{TSZ}} \delta \delta \delta \delta} D_l^{\text{TSZ;template}}, \quad \delta 4p$$

where  $f \delta x \approx 1 \times \coth \delta x = 2p - 4$  with  $x \approx \frac{1}{4} \ln \frac{T}{T_{\text{CMB}}}$  and we vary the amplitude parameter  $A^{\text{TSZ}}$  in the likelihood.

We model the correlation between the TSZ and CIB signals following George et al. [31] as

$$D_{l;v \times \mu}^{\text{TSZ-CIB}} \frac{1}{4} - \xi D_{l;v \times v}^{\text{TSZ}} D_{l;v \times v}^{\text{CIB-cl}} \beta D_{l;\mu \times \mu}^{\text{TSZ}} D_{l;\mu \times \mu}^{\text{CIB-cl}}; \quad \delta 5p$$

where  $\xi$  is the correlation parameter, which we vary in the likelihood. We define the sign here, such that  $\xi > 0$  corresponds to a reduction in power at 150 GHz.

<sup>7</sup>Note that while the choice of CIB temperature is different from Addison et al. [35], this has a negligible effect given that the SPT band passes are located in the Rayleigh-Jeans region of the spectrum [30,31].

Finally, we account for the kinematic Sunyaev-Zeldovich (KSZ) effect similar to Reichardt et al. [30] by rescaling a combined template for the homogeneous [37] and patchy [38] KSZ effects normalized at  $l \approx 3000$ , via

$$D_l^{\text{KSZ}} \frac{1}{4} A^{\text{KSZ}} D_l^{\text{KSZ;template}}, \quad \delta 6p$$

where we vary the amplitude parameter  $A^{\text{KSZ}}$  in the likelihood.

## 2. Polarization foregrounds

We adopt the polarization foreground model of D21. We account for Poisson sources in the EE power spectrum and polarized galactic dust in the EE and TE data. The priors for the former contaminant are unaltered from D21, while we amend priors on polarized galactic dust using the updated analysis of Planck data within our survey region (see Appendix A for details).

## C. External datasets

We use Planck data in combination with SPT-3G 2018 data to derive cosmological constraints. Planck and SPT-3G data complement one another by providing high-precision measurements of the CMB power spectra on large and small angular scales, respectively. Specifically, the SPT-3G data are more precise than Planck for TT at  $l > 2000$ , for TE at  $l > 1400$ , and for EE at  $l > 1000$ . We use the BASE\_PLIKHM\_TTTEEE\_LOWL\_LOWE Planck dataset [11].

We also report joint results for SPT-3G 2018 and WMAP data for key scenarios, to be as independent of Planck data as possible. We use the year nine dataset [15] with TT data at  $2 < l < 1200$ , and TE and EE data at  $24 < l < 800$ . We exclude polarization data at  $l < 24$ , due to the possibility of dust contamination [39], and include our baseline prior on  $\tau$  to constrain the optical depth to reionization instead. This setup is the same that Aiola et al. [5] used for joint ACT DR4 and WMAP constraints.

We ignore correlations between SPT-3G and satellite data. Planck and WMAP data cover a large amount of sky not observed by SPT. Moreover, the SPT-3G data are weighted towards higher  $l$ .

## IV. INTERNAL CONSISTENCY AND ROBUSTNESS OF RESULTS

In this section, we perform null tests, consistency tests on the final band powers, parameter-level consistency tests, and an assessment of the robustness of cosmological constraints. For each test category, we compute a set of probability-to-exceed (PTE) values, which we require to lie within some predetermined limits. We require the PTE values to lie above the threshold  $5\% = N$  for null tests and within the symmetric interval  $\frac{1}{2} \delta 2.5 = Np\%$ ;  $\delta 100 - 2.5 = Np\%$  for all other tests, where  $N$  is the number

of independent tests, i.e. using the Bonferroni correction for both cases, we find that the best-fit parameters in the look-elsewhere effect [40]. We determine  $N$  for each test category individually within the relevant section and conservatively do not correct for the look-elsewhere effect across different test categories as noted in Sec. II A, this work was done prior to unblinding parameter constraints.

### A. Null tests

We test that the data are free of significant systematic effects through six types of null tests. Following D21, we analyze the following data splits (to test for the corresponding category of systematic errors): azimuth (ground pick-up), first/second (chronological effects), left/right (scan-direction dependent effects), moon up/moon down (beam sidelobe pickup), saturation (decreased array responsivity), and detector module or “wafer” (nonuniform detector properties). The data are ranked or divided into groups based on a given possible systematic and we take the difference of these map bundles to form null maps. We then calculate the null spectra as the average of null map cross-spectra for each test and use their distribution to compute uncertainties. We verify that the average of these spectra is consistent with the expectation for a given test using a  $\chi^2$  statistic.

We update the null test framework employed by D21 as follows. First, we scale null spectra by  $|l| \propto 1/l^2$  and apply the debiasing kernel to the corresponding auto-frequency spectrum to the null spectra. This change corresponds to a linear transformation and does not change the pass state of tests while making it easier to interpret the amplitude of null spectra.

Second, we cast the TE and EE null spectra in nine bins of width  $\Delta l \approx 300$  spanning the angular multipole range  $300 < l < 3000$ , whereas for TT we use ten bins of width  $\Delta l \approx 250$  across  $750 < l < 3000$ . This change makes the tests more sensitive to plateaus in power. Furthermore, this allows us to ignore bin-to-bin correlations induced by the flat-sky projection step, which only drop to  $\leq 20\%$  for bins separated by  $\Delta l \geq 100$ .

Third, we add 1% of uncorrelated sample variance to the covariance of the TT null spectra. SPT-3G produces a high signal-to-noise measurement of the TT power spectrum. Minor low-level systematic effects may appear above the noise level, while having a negligible effect on cosmological results due to the high sample variance of the TT spectrum across the  $\sim 1500$  deg $^2$  field. We verify this by artificially displacing the final TT data band powers by vectors mimicking systematic effects and rerunning the temperature likelihood. We assess the potential impact of two potential systematic effects:

- (1) We assess the impact of unmodeled time constants by injecting a left-right expectation spectrum large enough to produce a null test failure.
- (2) We assess the impact of an overall miscalibration by increasing the amplitude of TT band powers by the square root of 1% of their total covariance.

For both cases, we find that the best-fit parameters in  $\Lambda$ CDM shift by  $< 0.2\sigma^{\text{TT}}$ , where  $\sigma^{\text{TT}}$  represents the size of parameter errors when using only TT data.

Fourth, we model the effect of detector time constants in the TT scan-direction expectation spectrum. The maps presented in D21 are not corrected for time constants, which we see in the scan-direction test. We model this null spectrum as a constant offset between left- and right-going scans of  $2vt$ , where we assume a uniform on-sky scan speed of  $v \approx 0.7$  deg s $^{-1}$  across the survey field and  $t \approx 4.6$  ms is the median time constant. This effect does not appear above the noise level in the TE and EE data. Detector time constants act as an effective beam. The maps used for the beam measurement in § IV E of D21 include this effect and therefore when we remove the instrument beam during the debiasing procedure we also remove the signature of detector time constants from the data band powers. The expectation spectrum for all other TT null tests is approximated as zero.

In addition to the individual TT, TE, and EE null tests, we also report results for all three spectra (TT=TE=EE) at a single frequency. We forego quantifying the correlation between the combined and individual tests and exclude this combined test in setting the PTE threshold. We assume that the remaining tests are independent from one another, such that across three frequencies and three spectrum types and six test categories, there are  $N \approx 3 \times 3 \times 6 \approx 54$  independent tests. We require all PTE values to lie above  $0.05 = 54 \approx 0.001$ . We do not repeat the meta-analyses (i.e. the per-row and full-table tests) carried out by D21 since the addition of sample-variance to the TT null spectra means the PTE values are not expected to be uniformly distributed. For this reason, we do not flag and investigate high PTE values in the TT and TT=TE=EE tests. Due to the updates detailed above we expect the PTE values of the TE and EE null tests to change from D21.

We report the null test PTE values in Table I. All of the PTE values lie above the set threshold. Across the 72 tests the lowest PTE value is 0.002 (EE 150 GHz Azimuth test). There is no significant mean change to the PTE values of the EE and TE reported in D21. The largest individual change is an increase to the PTE value of the TE 150 GHz Azimuth test by 0.683. We have confirmed that all PTE values also lie above the required threshold when adopting a finer bin width of  $\Delta l \approx 125$  for TT and  $\Delta l \approx 100$  for TE=EE null spectra.<sup>8</sup> We conclude that the data are free of significant systematic errors and proceed with the analysis.

### B. Power spectrum tests

In this section, we perform a series of power-spectrum level tests to assess the internal consistency of the SPT-3G 2018 TT=TE=EE dataset. We begin by combining the six

<sup>8</sup>The different bin widths are due to the different  $l$  ranges covered by temperature and polarization data.

TABLE I. Individual null test PTE values for 95, 150, and 220 GHz and TT, TE, and EE spectra. Additionally, we show the combined TT=TE=EE null test PTE values. All PTE values lie above the required threshold of  $0.05 = \delta 9 \times 6 \text{P} \approx 0.001$ .

	Azimuth	First/Second	Left/Right	Moon	Saturation	Wafer
95 GHz						
TT	0.116	0.614	0.630	0.991	0.882	0.492
TE	0.294	0.067	0.028	0.938	0.234	0.620
EE	0.765	0.398	0.015	0.866	0.340	0.037
TT=TE=EE	0.284	0.210	0.012	0.999	0.508	0.184
150 GHz						
TT	0.075	0.549	0.861	0.305	0.884	0.485
TE	0.879	0.539	0.859	0.894	0.238	0.465
EE	0.002	0.970	0.432	0.486	0.268	0.005
TT=TE=EE	0.012	0.882	0.889	0.667	0.460	0.045
220 GHz						
TT	0.310	0.548	0.635	0.635	0.128	0.077
TE	0.420	0.929	0.169	0.834	0.784	0.510
EE	0.991	0.735	0.222	0.835	0.875	0.501
TT=TE=EE	0.751	0.914	0.243	0.931	0.635	0.227

cross-frequency band power $\hat{D}$ , for each spectrum type into a minimum-variance combination $\hat{D}^{\text{MV}}$ , that represents our best foreground-free measurement of the CMB anisotropies. Following Planck Collaboration [41] and Mocanu et al. [42]

$$\hat{D}^{\text{MV}} \approx \frac{1}{4} \delta X^T C^{-1} X \delta^{-1} X^T C^{-1} \hat{D}; \quad \delta 7\text{P}$$

where  $C$  is the band power covariance matrix and  $X$  is the design matrix, which is populated with ones and zeros and connects the six cross-frequency estimates of the same signal per multipole bin in  $\hat{D}$  to the corresponding single element in  $\hat{D}^{\text{MV}}$  [41]. We subtract the best-fit foreground model from the data prior to the above procedure, though this only matters for the TT spectra since the foreground contamination in polarization is negligible.

For our first test, we compare the minimum-variance spectrum to the full set of multifrequency band powers and require that the PTE values lie within [2.5%, 97.5%] for each spectrum type and the full combination of TT=TE=EE spectra. This test ensures that the data are consistent with measuring the same underlying signal and free from any significant unmodeled foreground contamination. We use the test statistic

$$\chi^2 \approx \frac{1}{4} \delta \hat{D}^{\text{MV}} - \hat{D}^T C^{-1} \delta \hat{D}^{\text{MV}} - \hat{D} \delta; \quad \delta 8\text{P}$$

We obtain  $\chi^2 \approx 668$  for 605 degrees of freedom<sup>9</sup>. This corresponds to a PTE value of 4% for TT=TE=EE. For

TE, and EE spectra individually, we find PTE values of 22%, 12%, and 16%, respectively. The PTE value of the combined test is driven low by the 220 GHz data in temperature and polarization. However, all PTE values lie within the 95th percentile and we report no sign of significant internal inconsistency.

Second, we perform a conditional spectrum test to probe the interfrequency agreement within each spectrum type. This test is largely agnostic to the cosmological model, though it assumes that the foreground model describes the data well. We compare each self multifrequency band powers $\hat{D}^{\text{v}\mu}$ , where  $v, \mu$  denote the frequency combination, to the ensemble of other band powers of the same spectrum type. Following Planck Collaboration et al [11], we split the data band powers into  $\hat{D} \approx \hat{D}^{\text{v}\mu} + \hat{D}^{\text{others}}$ , where “others” indicates the part of the data we use for the prediction of the remainder. We decompose the best-fit spectrum,  $D$ , and the covariance,  $C$ , in the same way. The conditional prediction and the associated covariance are

$$\begin{aligned} & D^{\text{v}\mu; \text{cond}} \approx \frac{1}{4} D^{\text{v}\mu} \delta C^{\text{v}\mu \times \text{others}} \delta C^{\text{others} \times \text{others}}^{-1} \delta \\ & \times \delta \hat{D}^{\text{others}} - D^{\text{others}} \delta; \\ & C^{\text{v}\mu \times \text{v}\mu; \text{cond}} \approx \frac{1}{4} C^{\text{v}\mu \times \text{v}\mu} - C^{\text{v}\mu \times \text{others}} \\ & \times \delta C^{\text{others} \times \text{others}}^{-1} C^{\text{others} \times \text{v}\mu} \end{aligned} \quad \delta 9\text{P}$$

We compare this prediction to the measured data band powers using a<sup>2</sup> $\chi$  statistic and require all PTE values to lie within the interval  $\frac{1}{2} \delta 2.5 = N\text{P} \%, \delta 100 - 2.5 = N\text{P} \%$ , where  $N$  is the number of independent tests. Given that there are six cross-frequency combinations and three spectrum types, there are 18 tests in total. However, the number of independent tests is lower. We conservatively set  $N \approx 5$ ;

<sup>9</sup>We follow D21 and use the number of multifrequency band powers minus the number of minimum-variance band powers as the number of degrees of freedom.

due to the absence of correlated noise in the polarization data, the autofrequency EE tests are independent and we different spectrum types and probe the consistency between discount the remaining EE tests and assume that the TE the TT, TE, and EE data. In contrast to the per-frequency and TT tests only add one independent test each. We list conditional test, this test is dependent on the cosmological the PTE values and plot the results for the conditional model and we carry it out assuming  $\Lambda$ CDM. As in Planck residuals in Fig. 1. We find that all PTE values lie within the required interval; the conditional spectra are in good agreement with the measured data. This agreement is noteworthy, as across the different spectra we have data that are highly correlated (TT on intermediate scales) and uncorrelated beyond the common CMB sample variance (EE spectra).

Next, we apply the conditional test framework across the data, the autofrequency EE tests are independent and we different spectrum types and probe the consistency between discount the remaining EE tests and assume that the TE the TT, TE, and EE data. In contrast to the per-frequency and TT tests only add one independent test each. We list conditional test, this test is dependent on the cosmological the PTE values and plot the results for the conditional model and we carry it out assuming  $\Lambda$ CDM. As in Planck Collaboration et al. [11], this test is performed using the minimum-variance band powers. For each spectrum we compare the data minimum-variance combination to the conditional prediction given each other spectrum individually and jointly. We require all PTE values to lie within the interval  $\frac{1}{2}\delta 2.5 = Np\%$ ;  $\delta 100 - 2.5 = Nw\%$ , where  $N$  is the number of independent tests. Given the mild correlation

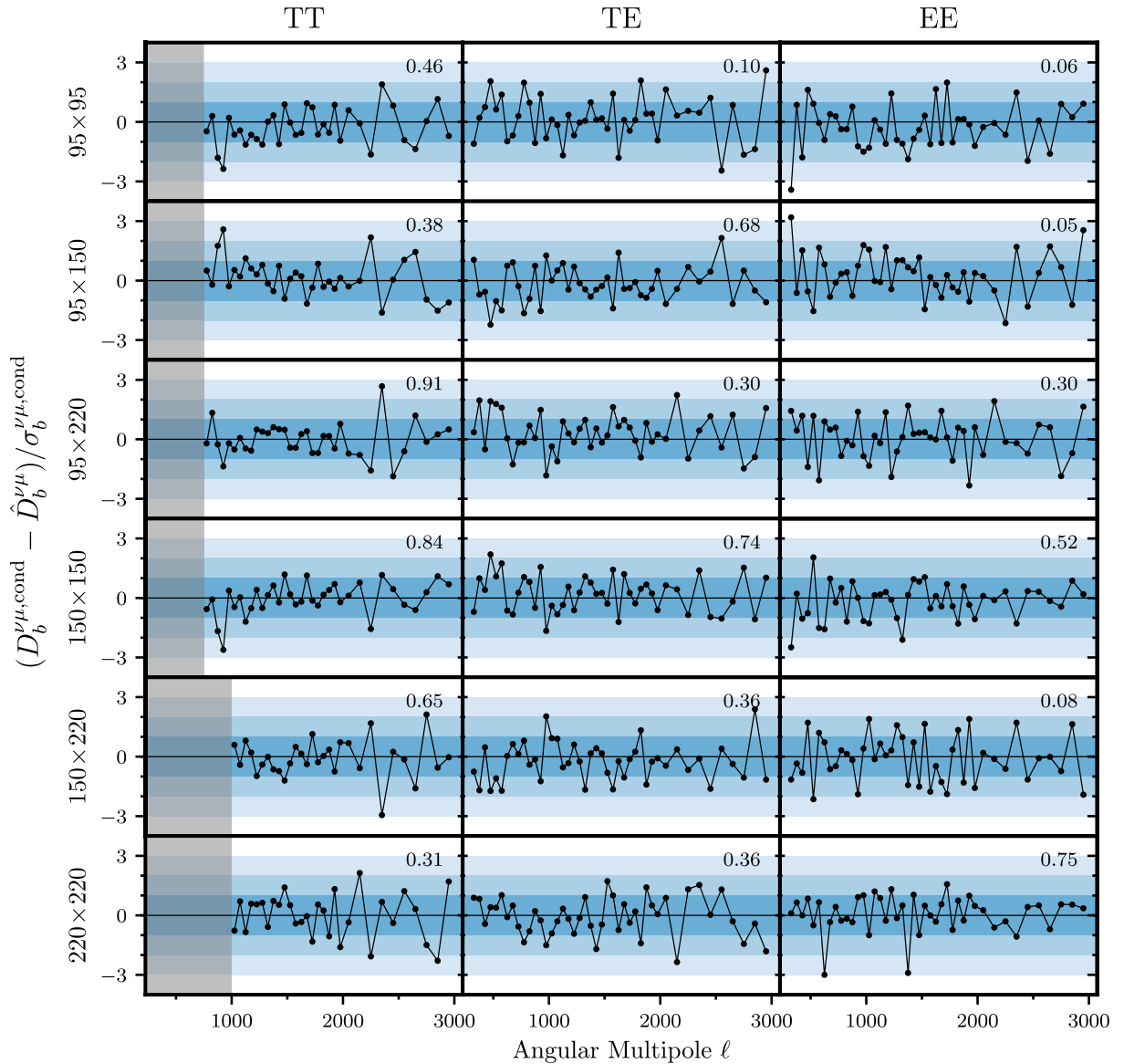


FIG. 1. Relative conditional residuals,  $\frac{(\hat{D}_b^{\nu\mu,\text{cond}} - \hat{D}_b^{\nu\mu})}{\sigma_b^{\nu\mu,\text{cond}}}$ , i.e. the difference between conditional predictions for a given set of multifrequency band powers and the measured data, divided by the square root of the diagonal of the conditional covariance. The blue shaded region corresponds to the  $3\sigma$  range and the gray shaded area in the first column indicates the TT angular multipole lower limit. The conditional residuals are consistent with zero, as evidenced by the PTE values indicated in the upper right corner of each panel. This speaks to the interfrequency consistency of the SPT-3G 2018 TT=TE=EE dataset.

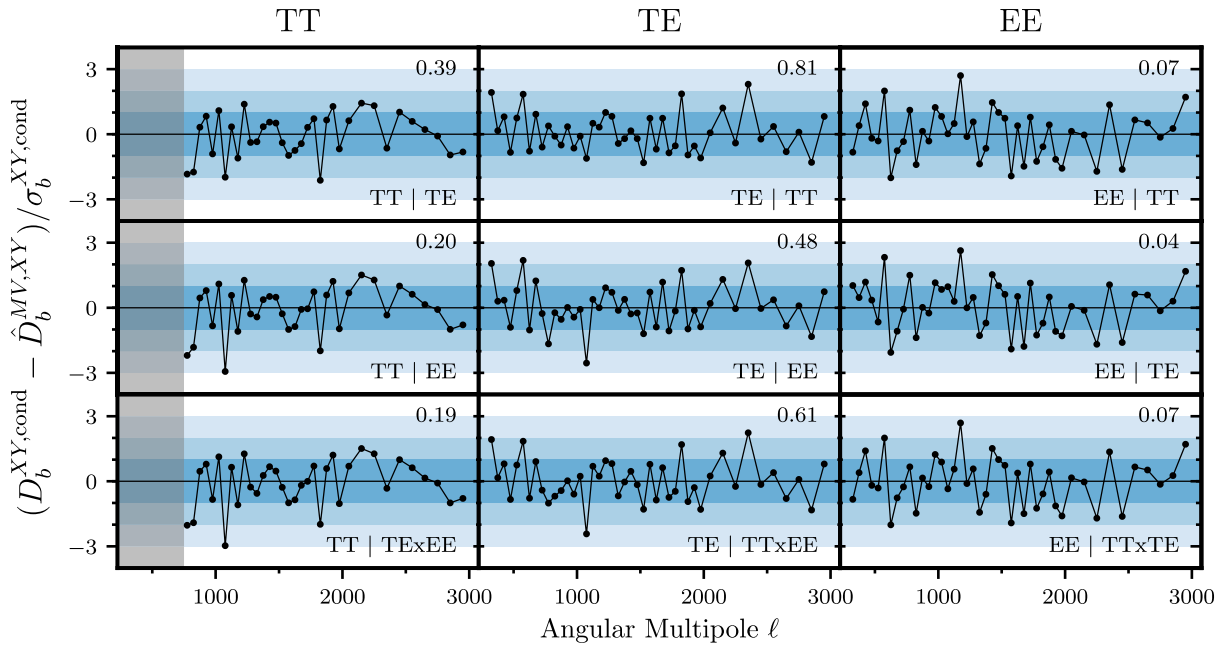


FIG. 2. Relative conditional residuals  $\delta D_b^{XY,cond} - \hat{D}_b^{MV,XY}$  with  $XY \in \{TT; TE; EE\}$ , i.e. the difference between conditional predictions for a given set of minimum-variance band powers and the measured data, divided by the square root of the diagonal of the conditional covariance. The blue shaded region corresponds to the  $3\sigma$  range and the gray shaded area in the first column indicates the TT angular multipole range. The spectra used in the conditional prediction are specified in the bottom right corner of each panel and the PTE values are indicated in the top right corner of each panel. We find good agreement between the different spectra of the SPT-3G 2018 TT=TE=EE dataset.

between the temperature and polarization anisotropies, which improves the numerical stability of the test by reducing the conservatively set  $N \approx 2$ . We show the conditional residuals in Fig. 2 and list the PTE values therein. We find no statistically significant outliers when comparing the conditional predictions and the measured data; all PTE values are in the required interval. The series of tests we have carried out provide a stringent assessment of the consistency of the SPT-3G 2018 TT=TE=EE band powers across frequencies and spectra; we conclude that the data are free of any significant internal tension at the power-spectrum level.

Though the tests above already complete our passing criteria to proceed with the analysis, we additionally investigate the difference spectra in Appendix D. This allows us to build further expertise with the data. We observe no significant features, such as slopes, constant offsets, or signal leakage.

### C. Parameter-level tests

We now turn to the internal consistency of the SPT-3G 2018 TT=TE=EE dataset at the parameter level. This test explicitly models dependent and independent parameters:  $\Omega^2$ ,  $\Omega_0 h^2$ ,  $\theta_{MC}$ ,  $n_s$ , and  $10^9 A_s \approx 0.1 \text{ Mpc}^3$ . Here,  $A_s \approx 0.1 \text{ Mpc}^3$  is the amplitude of the primordial power spectrum at  $k \approx 0.1 \text{ Mpc}^{-1}$ . This definition provides a better match to the scales constrained by the SPT data compared to the conventional reference point of  $k \approx 0.05 \text{ Mpc}^{-1}$  and

correlation between the combined amplitude parameter and  $n_s$ . We use the conventional reference point for  $A_s$  when reporting cosmological results in Sec. VI.

We investigate parameter constraints from the following subsets of the data: TT, TE, and EE spectra individually, or provide a stringent assessment of the consistency of the three sets of autofrequency spectra (95  $\times$  95 GHz, 150  $\times$  150 GHz, and 220  $\times$  220 GHz), large angular scales ( $l < 1000$ ), and small angular scales ( $l \geq 1000$ ). We follow Gratton and Challinor [43] and quantify the significance of the shift of mean parameter values from the full dataset to a given subset,  $\Delta p$ , using the parameter-level  $\chi^2$

$$\chi^2 \approx \Delta p^T C_p^{-1} \Delta p; \quad \delta 100 \approx$$

where  $C_p$  is the difference of the parameter covariances of the full dataset and a given subset. This formalism takes the correlation between parameters constraints from the full dataset and any given subset into account. As with the other tests, we require all PTE values to lie within  $\delta 2.5 = N\% = 100\%$ , where  $N$  is the number of independent tests. The large and small angular scale tests are independent from one another and we conservatively assume that the remaining six subsets only count as one independent test setting  $N \approx 3$ .

We plot parameter fluctuations for the standard  $\Lambda$ CDM parameters in Fig. 3 and list the subset  $\chi^2$  and associated

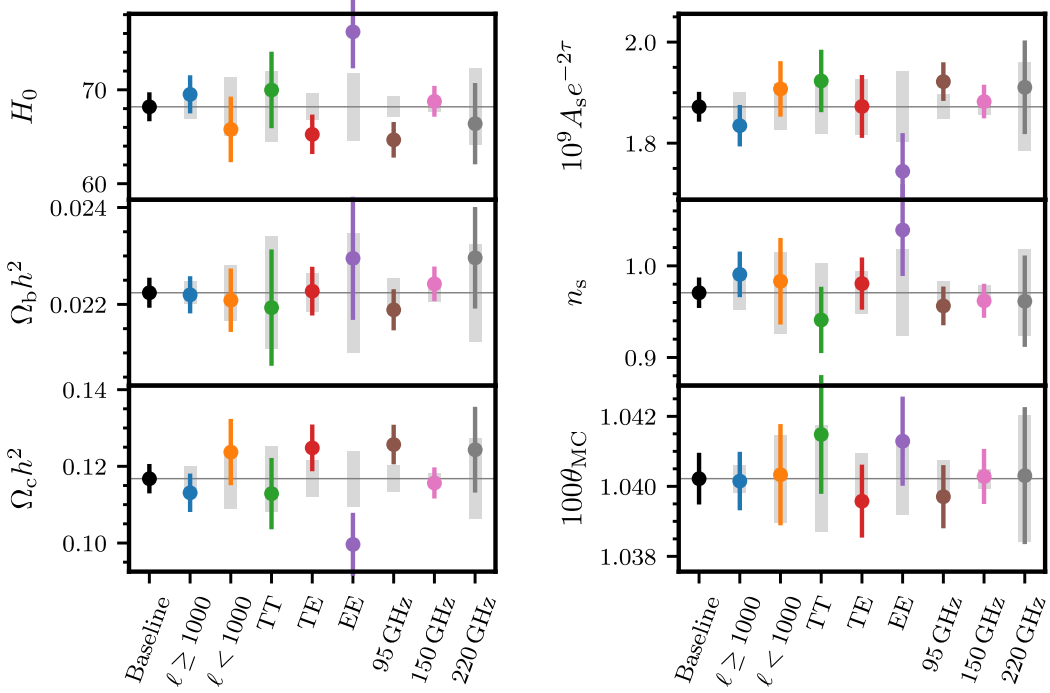


FIG. 3. Parameter constraints from the full SPT-3G 2018 TT=TE=EE dataset (black points) and select subsets (colored points as indicated) in  $\Lambda$ CDM. The gray boxes indicate the expected  $1\sigma$  fluctuations between each subset and the full dataset, taking the shared data into account. The observed shifts between subsets and the full data are consistent with statistical fluctuations. During the blind stage of this analysis, the parameter values along the vertical axes were not shown.

PTE values in Table II. We note that the EE parameter constraints deviate the most from the full dataset and have the lowest PTE value of any of the subsets. However, this PTE value is still above our preset criterion and we therefore consider the parameter shifts compatible with statistical fluctuations. We conclude that the data are internally consistent at the parameter level and proceed to unblind parameter constraints.

TABLE II. Parameter-level<sup>2</sup> and PTE values between subsets of the data and the full dataset. Note that there are five degrees of freedom as we perform the comparison across  $\Omega_b^2$ ,  $\Omega_c^2$ ,  $\Omega_{\text{MC}}^2$ ,  $10^9 A_s \delta k / 0.1 \text{ Mpc}^3 \text{ e}^{2\tau}$ ,  $n_s$ , due to the common  $\tau$  prior. Here, we use  $\delta k / 0.1 \text{ Mpc}^3$ , the amplitude of the primordial power spectrum at  $k / 0.1 \text{ Mpc}^{-1}$ , to improve the numerical stability of the test. All PTE values lie within the required interval of  $1\delta 2.5 = 3\%$ ;  $\delta 100 - 2.5 = 3\%$  and we conclude that the parameter shifts are compatible with statistical fluctuations.

Subset	$\chi^2$	PTE
$\ell \leq 1000$	4.8	44.7%
$\ell > 1000$	4.9	43.4%
TT	10.3	6.7%
TE	4.9	43.1%
EE	14.8	1.1%
95 GHz	9.8	8.0%
150 GHz	3.5	61.7%
220 GHz	1.9	86.5%

#### D. Robustness of cosmological constraints

We verify the robustness of our cosmological results with respect to variations of the likelihood presented in Sec. III. We test the following cases in  $\Lambda$ CDM: removing the priors on each set of amplitude parameters for a given foreground source; removing the priors on all temperature amplitude parameters simultaneously; widening the CIB spectral index prior by a factor of 2; introducing the CIB power law index as a free parameter either with a wide uniform prior or adopting the result of Addison et al. [35] as a prior; introducing CIB decorrelation parameters  $\zeta^v$  for each frequency band with uniform priors, between zero and unity that multiply Eq. (3) by  $\zeta^v \zeta^u$ ; ignoring the TSZ-CIB correlation; ignoring galactic cirrus; ignoring or quadrupling the beam covariance; adopting the  $\tau$  constraint found by Natale et al. [44] as a prior. In addition to these tests for constraints from the full TT=TE=EE dataset, we also investigate the effect of foreground model variations on constraints from TT alone. We find no significant change to cosmological constraints for any of the cases tested; all parameter shifts are  $< 0.3\sigma$ , where  $\sigma$  indicates the width of the respective TT=TE=EE or TT constraint using baseline priors.<sup>10</sup> We conclude that none of the likelihood variations

<sup>10</sup>We also test the case of removing all priors on foreground amplitude parameters when analyzing TT data alone in  $\Lambda$ CDM  $\beta_{\Lambda}$  and  $\Lambda$ CDM  $\beta N_{\text{eff}}$  and report no significant change to cosmological constraints.

above have a significant impact on cosmological constraints. Together with the consistency tests at the band power level in Sec. IV B, this indicates that our results are robust with respect to a mismodeling of the foreground contamination.

## V. THE SPT-3G 2018 POWER SPECTRA

We report the SPT-3G 2018 TT=TE=EE multifrequency band powers in Appendix C and plot the power spectrum measurement in Fig. 4. The SPT-3G 2018 TT power spectra are sample-variance dominated across the entire multipole range. The EE and TE band powers are sample-variance dominated for  $\ell < 1275$  and  $\ell < 1425$ , respectively. We report the minimum-variance band powers formed in Sec. IV B in Table III and plot them together with other power spectrum measurements in Fig. 5. Note that the minimum-variance band powers are only intended for plotting purposes and the likelihood uses the full set of multifrequency spectra. The uncertainty of the minimum-variance combination is reduced by 3%, 2–19%, and 4–31% compared to the  $150 \times 150$  GHz TT, TE, and EE band powers, respectively. This improvement is constant across scales for the sample-variance-limited TT spectra and increases at higher  $\ell$  for the noise-limited polarization spectra.

We can assess the relative weight of each multifrequency spectrum entering the minimum-variance contribution using

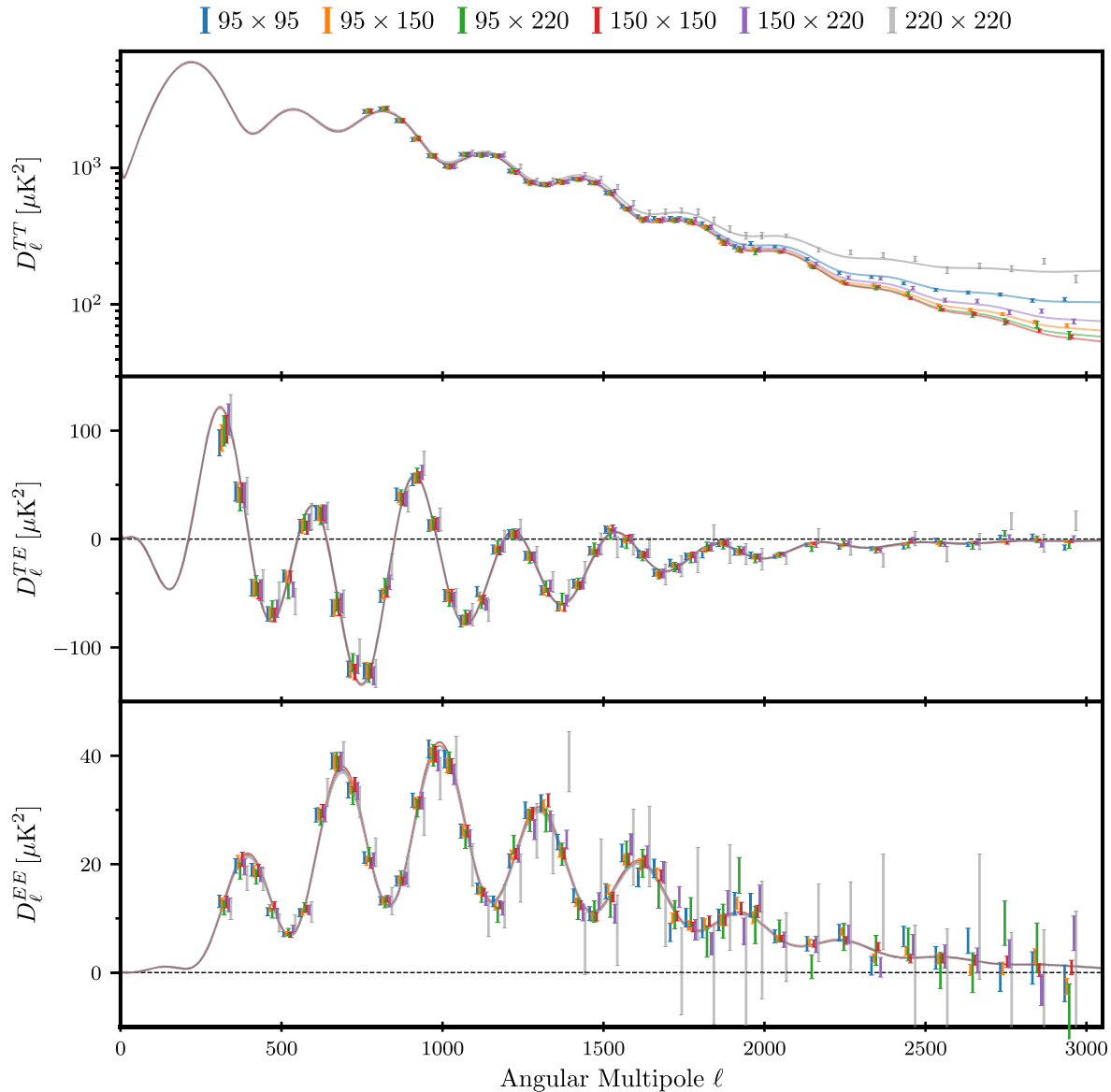


FIG. 4. SPT-3G 2018 multifrequency TT=TE=EE band powers in colors as indicated in the legend, along with the best-fit  $\Lambda$ CDM model to the SPT data including foregrounds (solid lines of matching color). The SPT-3G data provide a precision measurement of the CMB temperature and polarization anisotropies on intermediate and singular scales.

TABLE III. The SPT-3G 2018 TT=TE=EE minimum-variance band powers  $D_b$  and their associated uncertainties for each angular multipole bin. The band powers and errors are quoted in units of  $\mu\text{K}^2$ .

I Range	$D_b^{\text{TT}}$	$\sigma^{\text{TT}}$	$D_b^{\text{TE}}$	$\sigma^{\text{TE}}$	$D_b^{\text{EE}}$	$\sigma^{\text{EE}}$
300–350		92.96	10.32	12.87	1.02	
350–400		44.06	8.46	20.46	1.23	
400–450		−45.80	7.15	18.85	1.08	
450–500		−69.45	5.99	11.99	0.64	
500–550		−35.48	4.67	7.19	0.39	
550–600		11.07	5.70	11.42	0.61	
600–650		24.52	6.71	29.50	1.14	
650–700		−63.28	7.39	38.95	1.33	
700–750		−121.54	6.85	34.48	1.24	
750–800	2531.89	82.90	−121.56	6.65	20.80	0.88
800–850	2674.59	78.11	−50.31	4.71	13.47	0.55
850–900	2179.55	72.87	37.67	5.07	17.01	0.70
900–950	1578.46	52.45	56.22	4.89	31.37	1.05
950–1000	1201.33	38.99	13.95	4.83	40.44	1.33
1000–1050	1003.98	33.71	−51.61	5.19	38.49	1.30
1050–1100	1219.01	35.13	−74.30	4.69	26.27	0.96
1100–1150	1231.40	36.35	−54.77	3.82	15.05	0.64
1150–1200	1202.46	36.99	−10.53	3.28	12.34	0.59
1200–1250	907.07	28.30	4.39	3.30	21.73	0.85
1250–1300	771.75	22.69	−15.57	3.36	29.12	1.07
1300–1350	727.84	21.05	−47.79	3.42	31.14	1.08
1350–1400	771.56	24.02	−62.26	3.43	22.76	0.87
1400–1450	800.59	23.88	−42.49	3.04	12.82	0.65
1450–1500	748.60	21.56	−12.44	2.70	10.57	0.62
1500–1550	623.76	18.81	8.95	2.49	14.31	0.71
1550–1600	485.77	13.93	−0.16	2.53	21.27	0.86
1600–1650	404.60	12.95	−14.62	2.46	20.19	0.91
1650–1700	392.84	11.13	−32.37	2.25	18.27	0.81
1700–1750	393.10	12.46	−25.07	2.20	10.40	0.71
1750–1800	374.26	11.31	−15.43	2.05	8.78	0.65
1800–1850	353.00	10.17	−9.56	1.93	8.78	0.70
1850–1900	267.74	9.01	−3.44	1.89	9.95	0.77
1900–1950	227.93	7.76	−11.16	1.86	12.21	0.83
1950–2000	234.80	7.47	−16.46	1.83	11.11	0.82
2000–2100	222.41	3.97	−14.31	0.93	6.37	0.42
2100–2200	168.32	3.53	−4.86	0.87	5.28	0.44
2200–2300	120.67	2.64	−5.61	0.82	6.79	0.49
2300–2400	111.78	2.44	−9.24	0.80	3.49	0.51
2400–2500	88.87	2.16	−3.60	0.77	3.65	0.54
2500–2600	68.44	1.92	−3.78	0.75	2.54	0.59
2600–2700	60.31	1.78	−3.49	0.76	1.85	0.64
2700–2800	50.13	1.69	−2.32	0.78	1.63	0.71
2800–2900	38.42	1.55	−0.52	0.79	1.23	0.80
2900–3000	31.51	1.51	−2.48	0.82	−0.29	0.90

the diagonals of the mixing matrix,  $\delta X^T C^{-1} X P^{-1} X^T C^{-1}$ , which are shown in Fig. 6. Note that the absolute amplitudes of these elements correspond to the relative weights. The signs depend on the correlation structure and ensure that the sum of all elements is unity. We find that the  $95 \times 150$  GHz and  $150 \times 150$  GHz spectra generally dominate the minimum-variance combination. For TT, these spectra

combine to contribute 60% of the total weight at  $l \approx 1000$ , which increases to 91% at  $l \approx 3000$ . There is an abrupt change at  $l \approx 1000$ , i.e. when all multifrequency spectra are considered, while at larger angular scales the  $95 \times 150$  GHz frequency combination alone dominates the minimum-variance contribution. This is because (1) the  $95 \times 150$  GHz and  $150 \times 150$  GHz spectra are highly correlated on large angular scales while the former has a lower noise level and (2) the high degree of correlation between 150 and 220 GHz noise leads to a more complex interplay between data from all three frequency channels in the minimum-variance combination when the  $150 \times 220$  GHz and  $220 \times 220$  GHz spectra are available. For EE and TE, the  $95 \times 150$  GHz and  $150 \times 150$  GHz data contribute 65% and 79% at  $l \approx 300$  and 85% and 82% at  $l \approx 3000$ , respectively. Though the  $95 \times 150$  GHz and  $150 \times 150$  GHz data have a high combined weight, a wide frequency coverage is essential to control the foreground contamination and provides sensitivity to systematics.

## VI. COSMOLOGICAL CONSTRAINTS

### A. $\Lambda$ CDM

We report constraints on cosmological parameters in  $\Lambda$ CDM from SPT-3G 2018 TT=TE=EE in Table IV and show one- and two-dimensional marginalized posterior distributions in Fig. 7. The best-fit values for nuisance parameters all lie within  $2\sigma$  of the central value of their respective prior and are given in Appendix B. We show residuals between the minimum-variance data band powers and the best-fit model in Fig. 8 and plot the residuals for all multifrequency spectra in Appendix E.

We find that the  $\Lambda$ CDM model provides a good fit to the data. We report  $\chi^2 \approx 763.0$  across the 728 band powers of the full dataset. We ignore the effect of nuisance parameters and translate this  $\chi^2$  value to a PTE value of 15%. This agreement also applies to the three spectrum types individually. For TT, TE, and EE data we report  $\chi^2$  (PTE) values of 194.4(60%), 273.4(33%), and 285.5(17%), respectively.<sup>11</sup> All PTE values lie in the central 95th percentile, indicating the data are well fit by the standard model of cosmology.

The addition of temperature data to the TE=EE spectra noticeably improves constraints on all cosmological parameters as shown in Fig. 9. The posteriors of  $\Omega_b^2$ ,  $\Omega_c h^2$ ,  $\theta_{\text{MC}}$ ,  $10^9 A_s e^{-2r}$ , and  $\eta$  tighten by 8%, 12%, 8%, 27%, and 21%,

<sup>11</sup>While the foreground model helps improve the fit to the temperature data substantially, determining the effective number of degrees of freedom is not straightforward. If we conservatively account for 15 additional parameters, covering all baseline nuisance parameters,  $\bar{A}_s$ , the polarization foreground parameters, and the calibration parameters (following D21), we find a PTE value of 8% for the full dataset and 30% for TT. These values still indicate that  $\Lambda$ CDM provides a good fit to the data.

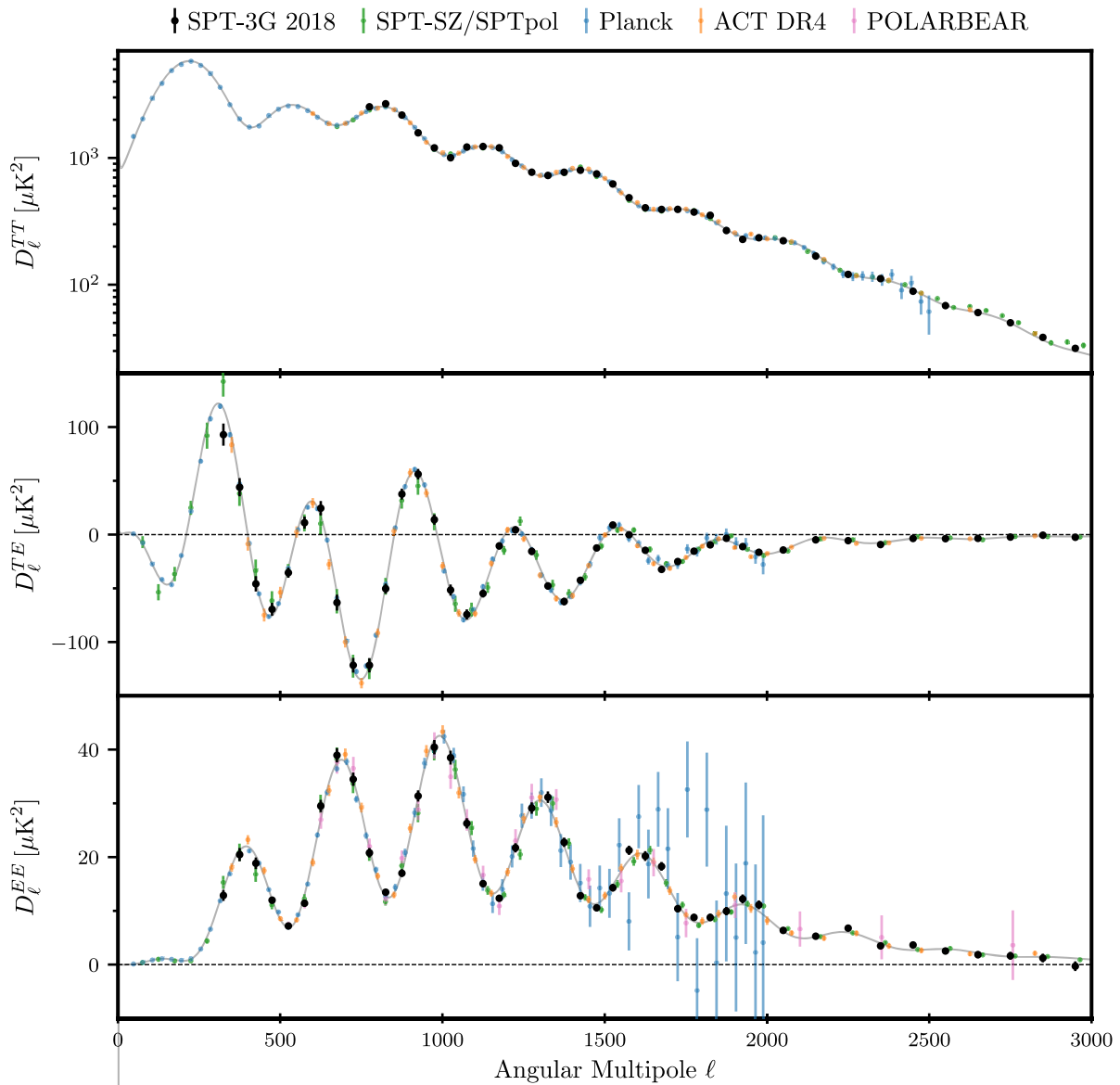


FIG. 5. SPT-3G 2018 minimum-variance  $TT=TE=EE$  band powers (black) along with a selection of contemporary power spectrum measurements: Planck (blue) [11], SPT-SZ (green, top panel only) [42], SPTpol (green, bottom two panels only, horizontally offset for clarity) [45], ACT DR4 (orange) [4] POLARBEAR (pink, bottom panel only) [46]. The SPT-3G 2018 best-fit CMB power spectrum is indicated in gray. The ensemble of CMB data is visually consistent and yields a high signal-to-noise measurement of the power spectrum.

respectively. The uncertainty on the  $H_0$  constraint shrinks by 12%. We use the determinant of the parameter covariance matrix as a metric for the allowed multidimensional volume. This value is in excellent agreement with the most recent results from Planck [1] and ACT [5]. Conversely, our result

as a metric for the allowed multidimensional volume lies  $2.6\sigma$  below the most precise local determination of finding a reduction of the five-dimensional allowed parameter space by a factor of 2.7. This value is in excellent agreement with the most recent results from Planck [1] and ACT [5]. Conversely, our result as a metric for the allowed multidimensional volume lies  $2.6\sigma$  below the most precise local determination of finding a reduction of the five-dimensional allowed parameter space by a factor of 2.7.

Constraints on the expansion rate today based on CMB data and supernovae and distance-ladder analyses are discrepant at the  $4 - 5\sigma$  level [1–3, 5, 47]. With SPT-3G 2018  $TT=TE=EE$  data we constrain the Hubble constant to

the Hubble constant, the Cepheid-calibrated supernovae distance-ladder analysis of Riess et al. [47], as can be seen in Fig. 10. The SPT-3G 2018  $TT=TE=EE$  dataset is effectively independent of Planck and ACT data so this result deepens the Hubble tension. Our  $H_0$  constraints are  $0.6\sigma$  below the distance-ladder analysis using the tip-of-the-red-giant-branch approach by Freedman et al. [48].

Moreover, it is  $2.1\sigma$  and  $1.0\sigma$  below the result of Wong et al. [49] and Birrer et al. [50] using strong-lensing time delays.

$$H_0 \approx 68.3 \text{ km s}^{-1} \text{ Mpc}^{-1}$$

023510-13

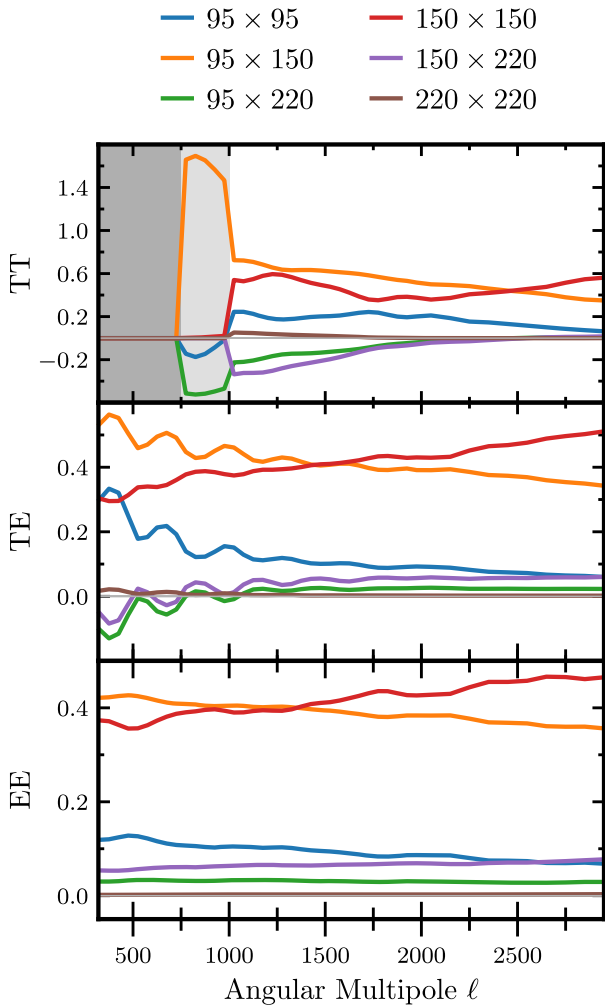


FIG. 6. Relative weight of each multifrequency spectrum entering the minimum-variance combination (diagonal elements of the mixing matrix). The gray shaded areas indicate the different  $l_{\min}$  cuts of the TT spectra. Overall, the  $95 \times 150$  GHz and  $150 \times 150$  GHz spectra contribute the most weight. For TT data, all spectra bar the  $220 \times 220$  GHz band powers are non-negligible at intermediate  $l$  and the  $95 \times 95$  GHz TE data are important on large angular scales.

Next, we look at structure growth as parametrized by the amplitude of matter fluctuations within a sphere with comoving volume of  $8 \text{ Mpc}^3$ ,  $\sigma_8$ , and the combined structure growth parameter  $\xi \propto \sigma_8 \Omega_m^{0.3}$ . The Planck constraint on  $\sigma_8$  using primary CMB data lies approximately  $3\sigma$  above the results of joint galaxy clustering and weak lensing analyses [1, 51, 52] as shown in the bottom panel of Fig. 11. For SPT-3G 2018 TT=TE=EE we report the following:

$$\sigma_8 \approx 0.797 \pm 0.015;$$

$$\xi \approx 12 \pm 0.042;$$

This result lies between  $\xi$  constraints from Planck data and low redshift data as shown in the top panel of Fig. 11; our central value is  $0.8\sigma$  below the Planck constraint [1] and  $0.5\sigma$  and  $0.7\sigma$  higher than the DES-Y3 [52] and KiDS-1000 [51] results, respectively. Adjusting our definition of  $\sigma_8$  appropriately, we find agreement at  $0.9\sigma$  with the SZ-cluster analysis of Bocquet et al [53].

We find the scalar spectral index of primordial fluctuations to be  $n_s \approx 0.970 \pm 0.016$ , which corresponds to a  $1.8\sigma$  preference for  $n_s < 1$ . We note that when excising our measurement of the third acoustic peak of the temperature power spectrum, i.e. TT data at  $l < 1000$ , we find  $n_s \approx 0.994 \pm 0.018$ . The corresponding five-dimensional parameter shift from the baseline result is a  $2.2\sigma$  event, where  $\sigma$  denotes the number of standard deviations equivalent to the associated PTE for a Gaussian distribution. This is compatible with a statistical fluctuation and we therefore expect that the addition of more data to the subset, i.e. our baseline configuration with TT data at  $l < 1000$ , yields constraints closer to the underlying mean. This matches what we observe when comparing to the tight constraints of Planck and WMAP [1, 55], which are enabled by the broad coverage of scales in log  $l$  space of satellite data adding TT data at  $l < 1000$  to the TTI  $> 1000 = \text{TE} = \text{EE}$  subset shifts our  $n_s$  result towards these tight constraints.

For a less model-dependent check on our TT measurement at  $750 < l < 1000$  we compare our minimum-variance band powers to the Planck full-sky power spectrum. Given that both datasets are sample-variance dominated on these angular scales, we assume that the SPT data are a subset of the Planck data; we use the difference of the SPT and Planck band power covariance matrices as the covariance of the difference between the two TT datasets.

We report a PTE value of 9%. This indicates that the two power spectrum measurements are in good agreement and we conclude that the effect the SPT-3G TT data at  $l < 1000$  has on  $n_s$  is not statistically anomalous.

We find excellent agreement between cosmological constraints from SPT-3G 2018 TT=TE=EE and Planck data. For individual  $\Lambda$ CDM parameters, all differences are  $< 1\sigma$ . Comparing all five parameters constrained by the SPT data, we find  $\chi^2 \approx 2.6$ , corresponding to a PTE value of 76%. This indicates a high level of agreement between the two datasets. This is particularly striking given that SPT-3G and Planck constraints are effectively independent of one another, given the large amount of sky observed by Planck that is not observed by SPT and the different weighting of the data as well as the different weightings of the TT, TE, and EE spectra. Though we use Planck data to calibrate our power spectrum measurement, we marginalize over the temperature calibration and polarization efficiency in the likelihood analysis. Furthermore, as per Sec. IV D we find that our cosmological results are robust when replacing the Planck-based prior on the optical depth to reionization with the result of Natale et al. [44]. The agreement between

TABLE IV. Marginalized constraints and 68% uncertainties on  $\Lambda$ CDM parameters from SPT-3G 2018 TT=TE=EE, along with joint constraints from SPT-3G 2018 TT=TE=EE + Planck, SPT-3G 2018 TT=TE=EE + WMAP, and results from Planck alone [1, 15]. We show constraints on the baseline  $\Lambda$ CDM parameters in the top half of the table combining the optical depth to reionization and amplitude of primordial fluctuations into  $10^9 \text{A}_s \text{e}^{-2\tau}$ . The bottom half shows select derived parameters. Note that we do not use WMAP polarization data at  $\ell < 24$  and SPT-3G data alone do not constrain the optical depth to reionization  $\tau$ ; instead, we use a Planck-based Gaussian prior of  $\tau \sim 0.0540 \pm 0.0074$ .

	SPT-3G 2018	SPT-3G 2018 + Planck	SPT-3G 2018 + WMAP	Planck
$\Omega_b h^2$	0.02224 $\pm$ 0.00032	0.02233 $\pm$ 0.00013	0.02240 $\pm$ 0.00020	0.02236 $\pm$ 0.00015
$\Omega_c h^2$	0.1166 $\pm$ 0.0038	0.1201 $\pm$ 0.0012	0.1171 $\pm$ 0.0027	0.1202 $\pm$ 0.0014
$100\theta_{MC}$	1.04025 $\pm$ 0.00074	1.04075 $\pm$ 0.00028	1.04016 $\pm$ 0.00067	1.04090 $\pm$ 0.00031
$10^9 A_s e^{-2\tau}$	1.871 $\pm$ 0.030	1.884 $\pm$ 0.010	1.867 $\pm$ 0.016	1.884 $\pm$ 0.012
$n_s$	0.970 $\pm$ 0.016	0.9649 $\pm$ 0.0041	0.9671 $\pm$ 0.0063	0.9649 $\pm$ 0.0044
$H_0$ [km s $^{-1}$ Mpc $^{-1}$ ]	68.3 $\pm$ 1.5	67.24 $\pm$ 0.54	68.2 $\pm$ 1.1	67.27 $\pm$ 0.60
$\sigma_8$	0.797 $\pm$ 0.015	0.8099 $\pm$ 0.0067	0.796 $\pm$ 0.012	0.8120 $\pm$ 0.0073
$S_8 \equiv \sigma_8 \sqrt{\Omega_m} = 0.3$	0.797 $\pm$ 0.042	0.832 $\pm$ 0.014	0.799 $\pm$ 0.031	0.834 $\pm$ 0.016
$\Omega_\Lambda$	0.700 $\pm$ 0.021	0.6835 $\pm$ 0.0075	0.698 $\pm$ 0.015	0.6834 $\pm$ 0.0084
Age=Gyr	13.815 $\pm$ 0.047	13.807 $\pm$ 0.021	13.804 $\pm$ 0.037	13.800 $\pm$ 0.024

SPT-3G and Planck data is not only a strong argument for the consistency and robustness of both experiments' cosmological results, but implies consistency of the  $\Lambda$ CDM model across angular scales and temperature and polarization spectra.

We find acceptable agreement between constraints from SPT-3G 2018 TT=TE=EE and ACT DR4. Across the five  $\Lambda$ CDM parameters constrained by the ground-based experiments, we find  $\chi^2/4 = 10.4$ , which translates to a PTE value of 6%. Interestingly, the largest difference is in  $\theta_{MC}$ , which controls the positions of acoustic peaks; CMB data constrain this parameter with great precision and SPT-3G 2018 TT=TE=EE yields a 0.07% measurement. ACT data yield a value  $2.0\sigma$  and  $1.7\sigma$  larger than SPT-3G and Planck data, respectively. Aiola et al. [5] note an offset in the cosmological parameter constraints on  $g$  and  $\Omega_bh^2$  when comparing Planck and ACT results (also visible in Fig. 7). Due to the degeneracy of these parameters with  $\theta_{MC}$ , the observed offset between ACT and SPT-3G constraints is likely related and from a similar origin. Regardless, the multidimensional test indicates that the observed parameter shifts are compatible with statistical fluctuations.

We report joint constraints from SPT-3G 2018 TT=TE=EE and Planck data in Table IV and find  $H_0 \approx 67.24 \pm 0.54 \text{ km s}^{-1} \text{ Mpc}^{-1}$ . This is a refinement of the Planck constraint on  $H_0$  by 11%. The precision measurement of the CMB anisotropies at small angular scales in temperature and polarization provided by SPT shrinks the Planck posteriors by approximately 10% for each  $\Lambda$ CDM parameter. Across the six-dimensional parameter space we report a reduction of the allowed volume factor of 1.7; for comparison, only adding the SPT TE=EE data to Planck leads to a reduction of the allowed parameter volume by a factor of 1.4. Due to the excellent agreement

SPT and Planck data, the shift to central values of parameter constraints compared to Planck alone is small. The SPT-3G 2018 data are in good agreement with WMAP and we report a PTE value for a five-dimensional parameter-space comparison of 95%. Combining the

SPT-3G and WMAP data yields constraints largely independent of Planck, which we list in Table IV. We report  $\Omega H_0 \approx 68.2 \pm 1.1 \text{ km s}^{-1} \text{ Mpc}^{-1}$ , which lies  $3.2\sigma$  below the distance-ladder analysis of Riess et al. [47] and deepens the Hubble tension. We report a constraint on the combined structure growth parameter of  $S_8^4 \approx 0.799 \pm 0.031$ , which is compatible with Planck, as well as DES Y3 and KiDS-1000 data and the SZ-cluster analysis of Bocquet et al. [53] within  $1\sigma$ . [1, 51, 52]. The addition of the low  $\ell$  power spectrum measurement of WMAP to SPT-3G data refines our  $n_s$  constraint by 62%. We report  $n_s^4 \approx 0.9671 \pm 0.0063$ , which disfavors a scale-invariant Harrison-Zel'dovich spectrum at  $5.2\sigma$ . For comparison, from WMAP data alone we infer  $n_s \approx 0.967 \pm 0.012$ , which is  $2.8\sigma$  from unity; the addition of SPT data tightens the constraint derived from WMAP data alone by 46%.

## B. Gravitational lensing, $A_l$

The lensing of CMB photons emitted at the surface of last scattering by intervening large scale structure causes a characteristic distortion of the CMB anisotropies leading to changes in the power spectrum: a smoothing of acoustic peaks and a transfer of power to the damping tail. Though the magnitude of this effect is derived from the values of cosmological parameters in the  $\Lambda$ CDM model, marginalizing over the effect of lensing on the primary CMB power spectra assesses the compatibility of the data with the standard model [56–58]. Planck Collaboration et al. [1] find a preference for increased lensing at  $2.8\sigma$ .

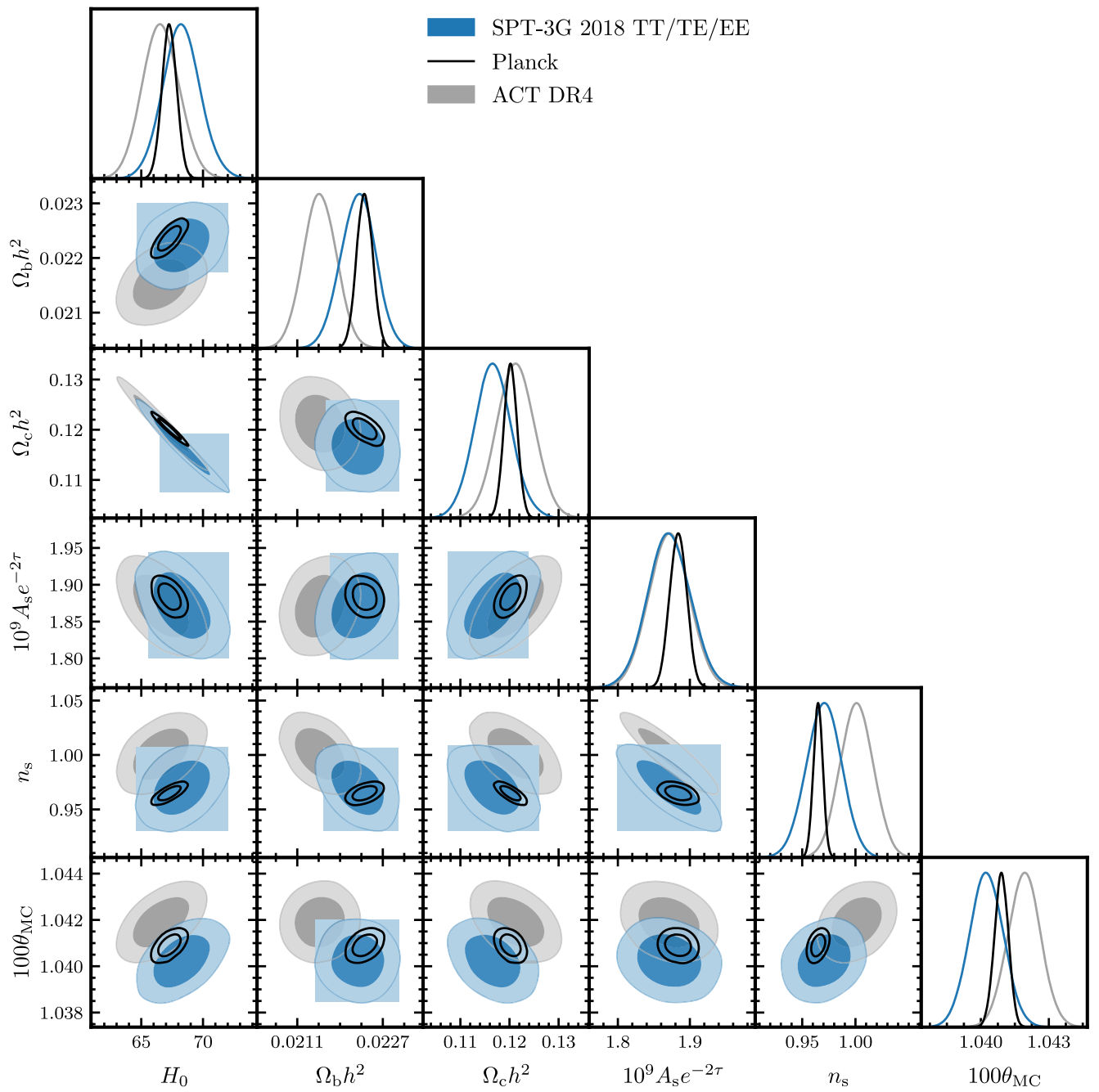


FIG. 7. Marginalized one- and two- dimensional posterior distributions for the SPT-3G 2018 TT=TE=EE dataset (blue contours), Planck (black line contours) and ACT DR4 (gray contours) in  $\Lambda$ CDM. The constraints derived from SPT-3G data are in excellent agreement with the Planck constraints, including for the SPT-3G and ACT data have similar constraining power and the differences in their constraints are compatible with statistical fluctuations.

We marginalize over an artificial scaling of the lensing power spectrum that smears the primary CMB,  $A_L$ , and report parameter constraints in Table V. We find

$$A_L \approx 0.87 \pm 0.11;$$

$$\delta \chi^2/13 \approx$$

which is compatible with the standard model prediction of unity at  $1.3\sigma$ . Adding  $A_L$  does not lead to a statistically significant improvement to the goodness of fit compared to  $\Lambda$ CDM ( $\Delta\chi^2/13 \approx 1.3$ ).

The SPT-3G 2018 TT band powers provide a sample-variance-limited measurement of the third and higher order acoustic peaks, which helps constrain cosmological

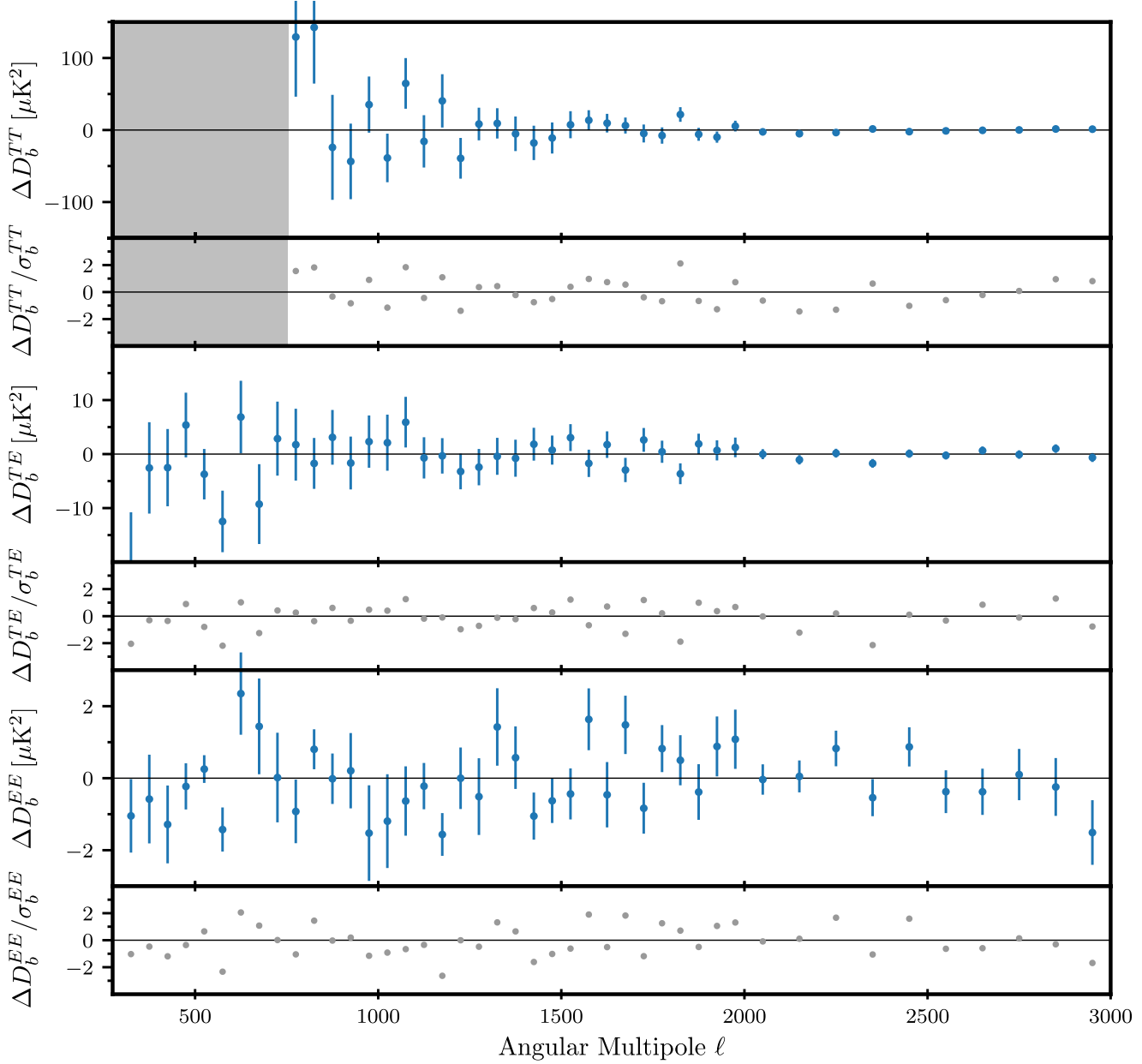


FIG. 8. Residuals of the SPT-3G 2018 TT=TE=EE minimum-variance data band powers to the best-fit  $\Lambda$ CDM model. Note that the SPT-3G band powers are correlated by up to 40% for neighboring bins. The standard model fits the data well and  $\chi^2 = 14768$  for  $\chi^2 = 723$  degrees of freedom. Residuals for the full array of multifrequency band powers are shown in Appendix E.

parameters in this model. The  $A_L$  constraint improves by 24% for TT=TE=EE compared to TE=EE as shown in Fig. 9. Across all six dimensions, the allowed parameter volume shrinks by a factor of 3.1.

In this model the SPT-3G and Planck constraints slightly diverge. Planck data yield  $A_L \approx 1.180 \pm 0.065$ , which is 2.5 $\sigma$  away from our result. Nevertheless, comparing the two datasets across the full six-dimensional parameter space gives  $\chi^2 \approx 10.2$ , which translates to a PTE value of 12% and indicates that the parameter shifts are consistent with statistical fluctuations.

We report joint constraints from SPT-3G 2018 and Planck data in Table V. We find  $A_L \approx 1.078 \pm 0.054$ , which is within 1.5 $\sigma$  of the standard model prediction. Adding SPT-3G to Planck data lowers the significance of the  $A_L$  constraint from unity and constraints on other cosmological parameters shift closer to the Planck only  $\Lambda$ CDM results. The width of the  $A_L$  posterior shrinks by 18% when adding SPT-3G to Planck data and the seven-dimensional allowed parameter volume decreases by a factor of 2.0.

We revisit the investigation of lensing convergence on the SPT-3G survey patch from Balkenhol et al. [3] using the

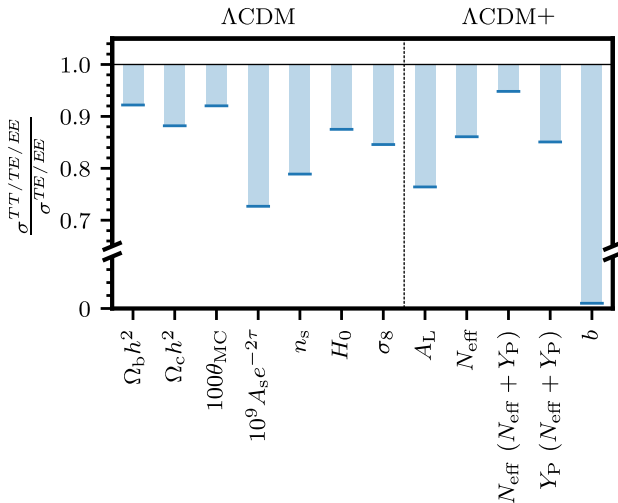


FIG. 9. Ratio of the widths of marginalized posteriors from SPT-3G 2018 TT=TE=EE and TE=EE for select  $\Lambda$ CDM parameters (left half) and extension parameters (right half). The addition of TT data leads to improvements on core  $\Lambda$ CDM parameters between 8–27% and the  $H_0$  and  $\sigma_8$  posteriors tighten by 12% and 15%, respectively. For  $\Lambda$ CDM  $\propto A_L$ ,  $\Lambda$ CDM  $\propto N_{\text{eff}}$ , and  $\Lambda$ CDM  $\propto N_{\text{eff}} \propto Y_P$  we report improvements for extension parameters between 5–24%. In the case of primordial magnetic fields,  $\Lambda$ CDM  $\propto b$ , TE=EE data alone suffers from a degeneracy between  $g$  and  $b$  and only the addition of TT data allows for a meaningful constraint. The vertical axis is split and the improvement on  $b$  shown only for visualization purposes.

complete SPT-3G 2018 TT=TE=EE dataset. We analyze joint constraints from SPT-3G 2018 and Planck data in  $\Lambda$ CDM foregoing the baseline Gaussian prior on  $\kappa$ . We adjust the sign of the  $\kappa$  definition in Sec. III to match Motloch and Hu [59] and the appendix of Balkenhol et al. [3]. We find

$$10^3 K_{\text{SPT-3G}}^{1/4} = -0.93 \quad 0.59: \quad \delta \Omega_8^{14\%}$$

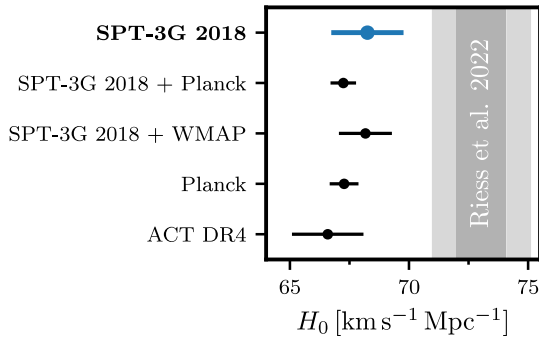


FIG. 10. Compilation of  $H_0$  constraints from combinations of different CMB datasets assuming  $\Lambda$ CDM: SPT-3G 2018, Planck [1], WMAP [15], ACT DR4 [5]. The vertical gray band indicates the 2 $\sigma$  constraint from the most precise supernovae and distance ladder analysis [47]. SPT-3G 2018 data allow for a precision constraint on  $H_0$  effectively independent from Planck data that deepens the Hubble tension.

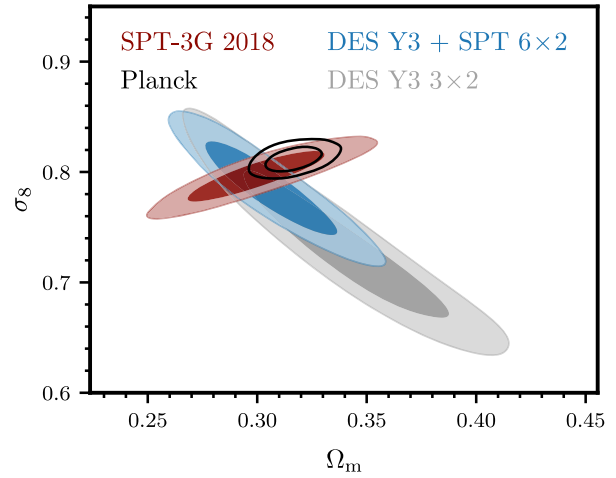


FIG. 11. Top panel: constraints in the  $\Omega_m$ – $\sigma_8$  plane from SPT-3G 2018 (red), Planck (black line), a joint analysis of DES Y3 galaxy position and lensing data and SPT and Planck CMB lensing data ( $6 \times 2$ , blue) [54], and DES Y3 joint galaxy density and weak lensing data ( $3 \times 2$ , gray) [52]. The combined structure growth parameter,  $S_8 \equiv \sigma_8 \sqrt{\Omega_m/0.3}$  varies perpendicular to the degeneracy direction of the DES data. Bottom panel: a compilation of  $S_8$  constraints using different cosmological datasets: SPT-3G 2018, Planck [1], WMAP [15], ACT DR4 [5], DES Y3 [52], DES Y3 + SPT [54], and KiDS-1000 [51]. Note that all constraints are produced assuming  $\Lambda$ CDM. The central value of the SPT-3G constraint lies between those of low-redshift analyses and Planck.

While the sign matches the result of Balkenhol et al. [3], our central value is compatible with zero at 1.6 $\sigma$ . We conclude that this test provides no significant evidence that the SPT-3G survey field aligns with a local density anomaly.

### C. Effective number of neutrino species, $N_{\text{eff}}$

Additional relativistic particles in the early universe, e.g., axionlike particles, hidden photons, gravitinos, massless

TABLE V. Constraints on  $\Lambda$ CDM model extensions  $N_{\text{eff}}$ , and  $N_{\text{eff}} + Y_P$  from SPT-3G 2018 TT=TE=EE alone and in combination with Planck data.

	A <sub>L</sub>		N <sub>eff</sub>		N <sub>eff</sub> + Y <sub>P</sub>	
	SPT-3G 2018	SPT-3G 2018 + Planck	SPT-3G 2018	SPT-3G 2018 + Planck	SPT-3G 2018	SPT-3G 2018 + Planck
$\Omega_b h^2$	0.02213 0.00033	0.02243 0.00015	0.02254 0.00046	0.02229 0.00020	0.02235 0.00050	0.02228 0.00020
$\Omega_c h^2$	0.1222 0.0060	0.1190 0.0014	0.1235 0.0089	0.1194 0.0028	0.139 0.018	0.1208 0.0042
$100\theta_{\text{MC}}$	1.03982 0.00081	1.04087 0.00029	1.03980 0.00092	1.04083 0.00039	1.0359 0.0030	1.0404 0.0011
$10^9 A_s e^{-2r}$	1.905 0.041	1.879 0.011	1.886 0.037	1.881 0.016	1.918 0.046	1.884 0.017
$n_s$	0.956 0.020	0.9677 0.0043	1.001 0.040	0.9628 0.0084	0.985 0.043	0.9630 0.0080
$A_L$	0.87 0.11	1.078 0.054				
$N_{\text{eff}}$			3.55 0.58	3.00 0.18	4.7 1.3	3.09 0.28
$Y_P$					0.165 0.058	0.238 0.016
$H_0$ [km s <sup>-1</sup> Mpc <sup>-1</sup> ]	66.1 2.3	67.73 0.64	71.7 4.3	66.9 1.4	77.5 7.2	67.4 1.7
$\sigma_8$	0.819 0.023	0.8031 0.0085	0.817 0.029	0.807 0.010	0.831 0.035	0.810 0.012
$S_8 \equiv \sigma_8 / \Omega_m = 0.3$	0.864 0.071	0.816 0.018	0.799 0.043	0.831 0.015	0.791 0.043	0.832 0.015
$\Omega_\Lambda$	0.666 0.037	0.6901 0.0087	0.713 0.026	0.6821 0.0098	0.727 0.029	0.6832 0.0098
Age=Gyr	13.861 0.058	13.789 0.024	13.36 0.54	13.86 0.19	12.59 0.89	13.78 0.25

Goldstone bosons, additional neutrino species as well as other forms of energy injection imprint on the CMB power spectra. At the parameter level, this modifies the effective number of neutrino species  $N_{\text{eff}}$ , which is 3.044 in the standard model [60–64].

We report constraints on the  $\Lambda$ CDM +  $N_{\text{eff}}$  model in Table V, finding

$$N_{\text{eff}} \approx 3.55 \pm 0.58; \quad \delta 15\%$$

This result is compatible with the standard model prediction at  $0.9\sigma$ . The best-fit  $\Lambda$ CDM +  $N_{\text{eff}}$  model does not improve on the good fit to the SPT-3G data achieved by  $\Lambda$ CDM significantly ( $\Delta\chi^2 \approx -0.2$ ).

The addition of sample-variance-limited measurements of the damping tail of the TT power spectrum improves on the cosmological constraints achieved by SPT-3G 2018 TE=EE in this model. As shown Fig. 9, the posterior of  $N_{\text{eff}}$  tightens by 14% when adding the SPT-3G 2018 TT band powers. The allowed volume across the full six-dimensional parameter space shrinks by a factor of 2.8.

We find good agreement in  $N_{\text{eff}}$  between the SPT-3G and Planck data with the central values separated by 1.0. Comparing all six parameters simultaneously, we find  $\chi^2 \approx 3.3$ , which translates to a PTE value of 77%. The parameter constraints are compatible with statistical fluctuations.

We list joint constraints from SPT-3G 2018 and Planck in Table V and report  $N_{\text{eff}} \approx 3.00 \pm 0.18$ . This constraint on the effective number of neutrino species is in excellent agreement with the standard model prediction of 3.044 ( $0.2\sigma$ ). While the addition of the SPT-3G to the Planck dataset only leads to a marginal improvement of the  $N_{\text{eff}}$  constraint (4%), the allowed seven-dimensional parameter volume is reduced by a factor of 1.5.

#### D. Effective number of neutrino species and primordial helium abundance, $N_{\text{eff}} + Y_P$

Varying  $N_{\text{eff}}$  alone assumes that any additional relativistic species present at recombination were also present at big bang nucleosynthesis. By simultaneously marginalizing over the primordial helium abundance, we remove this assumption and flexibly probe the relativistic energy density in the early Universe [63,65].

We present constraints from SPT-3G 2018 TT=TE=EE in Table V. We report

$$N_{\text{eff}} \approx 4.7 \pm 1.3; \quad \delta 16\%$$

The central values of the  $N_{\text{eff}}$  and  $Y_P$  constraints are compatible with the standard model predictions at  $1.3\sigma$  and  $1.4\sigma$ , respectively. We report no significant improvement to the goodness of fit for this model over  $\Lambda$ CDM ( $\Delta\chi^2 \approx -2.1$  for two additional parameters).

Comparing the determinants of the parameter covariances when using TT=TE=EE vs TE=EE data, we find that the allowed parameter volume is reduced by a factor of 2.4 through the inclusion of temperature band powers. The  $N_{\text{eff}}$  and  $Y_P$  uncertainties shrink by 5% and 15%, respectively, which we show in Fig. 9.

Again, we find good agreement between SPT-3G and Planck data in this model: across the full seven-dimensional parameter space we report  $\chi^2 \approx 4.5$ , which translates to a PTE value of 72%. The  $N_{\text{eff}}$  and  $Y_P$  constraints of the two datasets are compatible at  $1.4\sigma$  and  $1.3\sigma$ , respectively. We conclude that the differences in parameter constraints are compatible with statistical fluctuations.

Joint constraints from SPT-3G 2018 and Planck are given in Table V. We report  $N_{\text{eff}} \approx 3.09 \pm 0.28$  and  $Y_P \approx 0.238 \pm 0.016$ . The central values of the joint

TABLE VI. Constraints on primordial magnetic fields from SPT-3G 2018 TT=TE=EE alone and in combination with Planck data. For consistency, we report results for  $\Omega_b h^2$  however, the assumptions around recombination used in this approximation to the sound horizon fail in this model [24]. Hence, we also report results for the accurate angular scale of the sound horizon at recombination,  $100\theta$ .

	SPT-3G 2018		SPT-3G 2018 + Planck	
$\Omega_b h^2$	0.02216	0.00032	0.02234	0.00013
$\Omega_c h^2$	0.1185	0.0039	0.1210	0.0013
$100\theta_{MC}$	1.0475	0.0049	1.0442	0.0024
$10^9 A_s e^{-2\tau}$	1.87	0.03	1.8830	0.0097
$n_s$	0.964	0.017	0.9610	0.0043
$b$	$<1.0$		$<0.37$	
$H_0$ [km s $^{-1}$ Mpc $^{-1}$ ]	70.0	1.9	68.10	0.74
$\sigma_8$	0.809	0.017	0.8137	0.0065
$S_8$	0.794	0.041	0.828	0.012
$\Omega_\Lambda$	0.710	0.021	0.6894	0.0076
Age=Gyr	13.62	0.14	13.706	0.071
$100\theta$	1.04040	0.00075	1.04086	0.00029

SPT-3G and Planck  $N$  and  $Y_p$  constraints lie within  $0.2\sigma$  and  $0.5\sigma$  of their standard model predictions, respectively, and improve on the Planck only results by 9% and 8%, respectively. Across the full eight-dimensional parameter space, the addition of SPT-3G to Planck data leads to a reduction of the allowed parameter volume by a factor of 1.8.

### E. Primordial magnetic fields

The presence of primordial magnetic fields (PMFs), i.e. magnetic fields prior to recombination, increases the inhomogeneity of the baryon density,  $\rho_b$ . This so-called baryon clumping effect is parametrized by  $b \equiv \delta h_b^2 - h_b^2 b^2 = h_b^2$ , such that  $b \approx 0$  corresponds to no PMFs. With other cosmological parameters fixed, increasing  $b > 0$  changes the width of the visibility function and shifts it to higher redshifts, i.e. recombination occurs sooner, which leads one to infer higher values of  $H_0$  from CMB data [17, 66–68]. Because the distribution of baryons in the early Universe is not known precisely, we use the three-zone toy model put forward by Jedamzik and Abel [66] and Jedamzik and Pogosian [68].

We list constraints on  $\Lambda$ CDM  $b$  from the SPT-3G 2018 TT=TE=EE data in Table VI and show the marginalized one-dimensional posterior for  $b$  in Fig. 12. We find a 95% confidence upper limit of

$$b < 1.0:$$

$$\delta 17\sigma$$

The tight limit on the PMF-induced baryon clumping limits the possibility of resolving the Hubble tension through

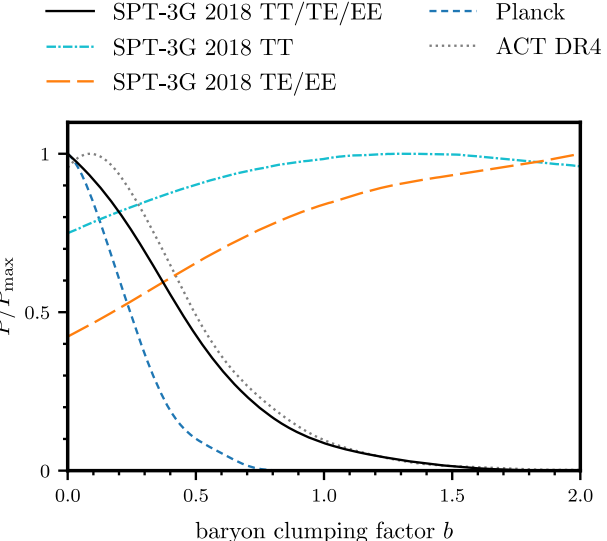


FIG. 12. Marginalized one-dimensional posterior distributions for the SPT-3G 2018 TT=TE=EE (black solid line), TT (light blue dash-dotted line), and TE=EE (orange long dashed line) on the clumping factor  $b$  induced by primordial magnetic fields. We also show the constraints from Planck primary CMB and lensing data (dark blue shortdashed line) and ACT DR4 (gray dotted line). The combination of TT and TE=EE spectra allows us to break degeneracies and set a tight constraint on  $b$ . The SPT-3G and ACT data have similar constraining power.

this model; we find  $H_0 \approx 70.0$  km s $^{-1}$  Mpc $^{-1}$ , which remains  $1.3\sigma$  below the distance-ladder analysis of Riess et al. [47]. We find no improvement to the goodness of fit for this model compared to  $\Lambda$ CDM ( $\Delta \chi^2 \approx 0$ ).

Measurements of the full TT=TE=EE power spectra are crucial in this model. Galli et al. [17] point out a degeneracy between  $b$  and  $n_s$ ;  $10^9 A_s e^{-2\tau}$  that prohibits meaningful constraints on  $b$  if only TT or only TE=EE power spectrum measurements are available (see Fig. 10 therein). Therefore, while Galli et al. [17] report an effective nonconstraint on  $b$  using the SPT-3G 2018 TE=EE dataset of D21, the addition of TT data in this work allows for a meaningful constraint, which we visualize in Fig. 9.

Due to the sensitivity of the  $b$  constraint to the values inferred from temperature and polarization data we confirm that our result is consistent with expectations based on simulations. The upper limit we report for the data is within 20% of what we infer from simulated band powers centered on  $b \approx 0$ .

We find good agreement between SPT-3G and Planck constraints in this model. Across the full seven-dimensional parameter space we report  $\chi^2 \approx 2.3$ , which translates to a PTE value of 88%. We report joint constraints from SPT-3G 2018 and Planck data on  $\Lambda$ CDM  $b$  in Table VI. We find a 95% confidence upper limit of  $b < 0.37$ . The addition of the SPT-3G data to Planck tightens the  $b$  upper

limit by 40% and reduces the volume of the allowed parameter space by a factor of 2.5.

## VII. CONCLUSION

In this work, we present a measurement of the CMB temperature power spectrum using SPT-3G data recorded in 2018. The TT band powers are sample-variance limited across the reported angular multipole range of  $750 < l < 3000$ . Together with the already published polarization data [D21] from the same observing season, this completes the SPT-3G 2018 TT=TE=EE dataset. We analyze the internal consistency of the data using a variety of tools: null tests, difference spectra, complement spectra (across frequencies and spectrum types), MV comparisons, and parameter-level subset tests. We find good agreement across frequencies, spectrum types and angular multipoles.

We present cosmological parameter constraints from the SPT-3G 2018 TT=TE=EE band powers. This is the first analysis using SPT-only measurements of all three primary CMB power spectra and the complete dataset provides the strongest constraining power to date from SPT. The data are well fit by  $\Lambda$ CDM with a PTE value of 15%. We constrain the expansion rate today to  $H_0 = 68.3 \pm 1.5 \text{ km s}^{-1} \text{ Mpc}^{-1}$ , the combined structure growth parameter  $\sigma_8 = 0.797 \pm 0.042$ , and find a preference for  $n_s < 1$  at  $1.8\sigma$ . The addition of the SPT-3G temperature power spectrum measurement to the TE=EE data improves cosmological parameter constraints by 8–27% and reduces the allowed five-dimensional parameter volume by a factor of 2.7. We report excellent agreement between the SPT-3G and Planck data with deviations of  $< 1\sigma$  for all cosmological parameters. Adding the SPT-3G band powers to the Planck primary power spectrum measurement leads to a reduction of the allowed six-dimensional parameter volume by a factor of 1.7.

We consider a series of extensions to the standard model drawing on the following parameters: the strength of gravitational lensing affecting the primary CMB power spectra,  $A_L$ , the effective number of neutrino species,  $N_{\text{eff}}$ , the primordial helium abundance,  $Y_P$ , and the baryon-clumping induced by primordial magnetic fields,  $b$ . We do not find a preference for any of these extensions over the standard model. The addition of temperature to TE=EE power spectrum measurements leads to significant improvements on cosmological constraints. For  $\Lambda$ CDM  $b A_L$ ,  $\Lambda$ CDM  $b N_{\text{eff}}$ , and  $\Lambda$ CDM  $b N_{\text{eff}} b Y_P$ , the posterior widths of extension parameters shrink by 5–24% and the multidimensional allowed parameter volume decreases by factors of 2.4–3.1. In the case of primordial magnetic fields, the combination of temperature and polarization data is essential to break degeneracies between  $b$  and  $n_s$ ;  $10^9 A_s e^{-2r}$  [17]. We find a 95% confidence upper limit on the PMF-induced baryon clumping from the Albert Shimmens Fund. The McGill authors

of  $b < 1.0$ . Our findings reflect that joint analyses of TT=TE=EE power spectrum measurements yield a substantial increase in constraining power over TE=EE alone; this approach is key to distinguishing between significant deviations from the standard model and statistical fluctuations and provides further ways to test the data for systematic effects.

The framework presented here will be used for ongoing analyses of SPT-3G data recorded in the 2019 and 2020 observing seasons. These observations include measurements of the same  $\sim 1500 \text{ deg}^2$  survey field used here, but achieve a map noise  $\sim 3.5 \times$  smaller. Moreover, extended survey data from these seasons cover an additional  $\sim 2800 \text{ deg}^2$ , reducing sample variance and improving measurements of the power spectrum on large angular scales. The combined SPT-3G measurements presented in this work represent a significant improvement for cosmological constraints from ground-based CMB data and are an important demonstration for future experiments, such as CMB-S4 [69].

## ACKNOWLEDGMENTS

We thank Karsten Jedamzik and Levon Pogosian for their help with models featuring baryon clumping due to primordial magnetic fields. The South Pole Telescope program is supported by the National Science Foundation (NSF) through Awards No. OPP-1852617 and No. OPP-2147371. Partial support is also provided by the Kavli Institute of Cosmological Physics at the University of Chicago, Argonne National Laboratory, and the University of Chicago. Argonne National Laboratory's work was supported by the U.S. Department of Energy, Office of High Energy Physics, under Contract No. DE-AC02-06CH11357. Work at Fermi National Accelerator Laboratory, a DOE-OS, HEP User Facility managed by the Fermi Research Alliance, LLC, was supported under Contract No. DE-AC02-07CH11359. The Cardiff authors acknowledge support from the UK Science and Technologies Facilities Council (STFC). The IAP authors acknowledge support from the Centre National d'Études Spatiales (CNES). This project has received funding from the European Research Council (ERC) under the European Union's Horizon 2020 research and innovation programme (Grant Agreement No. 101001897). This research used resources of the IN2P3 Computer Center [70]. M. A. and J. V. acknowledge support from the Center for AstroPhysical Surveys at the National Center for Supercomputing Applications in Urbana, IL. J. V. acknowledges support from the Sloan Foundation. K. F. acknowledges support from the Department of Energy Office of Science Graduate Student Research (SCGSR) Program. The Melbourne authors acknowledge support from the Australian Research Council's Discovery Project scheme (Grant No. DP210102386). L. B. acknowledges support from the Albert Shimmens Fund. The McGill authors

TABLE VII. Comparison of marginalized constraints and 68% errors of  $\Lambda$ CDM free and derived parameters from SPT-3G 2018 TE=EE data using the originahd updated likelihood.

	SPT-3G 2018 TE=EE (Original)		SPT-3G 2018 TE=EE (Updated)	
$\Omega_b h^2$	0.02241	0.00032	0.02218	0.00035
$\Omega_c h^2$	0.1152	0.0037	0.1145	0.0043
$100\theta_{MC}$	1.03963	0.00073	1.04013	0.00081
$10^9 A_s e^{-2r}$	1.811	0.040	1.800	0.041
$n_s$	1.000	0.019	1.008	0.021
$H_0$ [km s <sup>-1</sup> Mpc <sup>-1</sup> ]	68.7	1.5	69.0	1.7
$\sigma_8$	0.788	0.016	0.786	0.018
$S_8 \equiv \sigma_8 / \Omega_m = 0.3$	0.779	0.042	0.772	0.047
$\Omega_\Lambda$	0.706	0.021	0.710	0.023
Age=Gyr	13.809	0.049	13.813	0.052

acknowledge funding from the Natural Sciences and Engineering Research Council of Canada, Canadian Institute for Advanced Research, and the Fonds de recherche du Québec Nature et technologies. The UCLA and MSU authors acknowledge support from Grants No. NSF AST-1716965 and NoCSSI-1835865A. S. M. is supported by the Mullard Space Science Laboratory (MSSL) STFC Consolidated Grant. This research was done using resources provided by the Open Science Grid [71, 72], which is supported by the NSF Award No. 1148698, and the U.S. Department of Energy's Office of Science. Some of the results in this paper have been derived using the HEALPY and HEALPix<sup>12</sup> packages [73, 74]. The data analysis pipeline also uses the scientific PYTHON stack [75–77].

#### APPENDIX A: UPDATES TO THE POLARIZATION ANALYSIS PIPELINE

We make two key updates to the analysis of the TE=EE spectra from D21, which primarily update the covariance matrix. First, we account for correlated noise across frequencies. Extending the work in D21, we take the difference between two half-depth coadded maps at different frequencies. We divide the power spectrum of this difference map by the square root of the product of the power spectra of the corresponding autofrequency noise spectra. This yields an estimate of the correlation coefficient of the noise between two frequency channels. We find that for intensity the 95 and 150 GHz channels, as well as the 95 and 220 GHz channels, are moderately correlated with  $p \approx 0.6$  at  $l \leq 750$  and  $p \leq 0.2$  at  $l \geq 2000$ . The 150 and 220 GHz channels are highly correlated with  $p \approx 0.9$  at  $l \leq 750$  and  $p \leq 0.4$  at  $l \geq 2000$ . This correlation is high compared to past and contemporary ground-based CMB

experiments, due to the novel trichromatic architecture of SPT-3G pixels [19]. The behavior with  $l$  matches the expectation that only atmospheric noise is correlated across frequencies not instrumental noise. The different degrees of correlation are a consequence of a water emission line at 183 GHz and an oxygen line at 119 GHz [78, 79]. We use the correlation coefficients derived in this way to update the noise model in the covariance calculation (see § IV H in D21 for details). We detect no correlated noise across frequencies in polarization or correlated noise between temperature and polarization.

Second, we use a series of 1,000 simulations to update the mode-coupling model in the covariance calculation. The Lambert azimuthal equal-area projection does not preserve angles and leads to increasing bin-to-bin correlations at high  $l$ . For each simulation, we generate a CMB-only HEALPix sky, mask the map using the data apodization mask, and project the curved-sky map into a flat-sky map. We estimate the correlation matrix using the scatter of the power spectra of the 1,000 flat-sky maps. The recovered correlation structure matches the data well and is less noisy than the data estimate due to the increased number of independent realizations. Following D21, we fit second-order polynomials to band-diagonal elements of the correlation estimate from simulations and use these fits in the data correlation matrix. While in principle filtering effects not captured by these simulations lead to off-diagonal elements in the covariance matrix, the correlation structure of the data is completely dominated by the flat-sky projection.

We compare parameter constraints from the original TE=EE likelihood to the updated version in Table VII and Fig. 13. The central values of cosmological parameter constraints shift by less than the size of the new error bars. The parameter uncertainties generally widen with the updated covariance, by at most 15% for  $\Omega_c h^2$ . The addition of TT data to the updated covariance allows for as good as or better parameter constraints than reported in D21.

<sup>12</sup><http://healpix.sf.net/>.

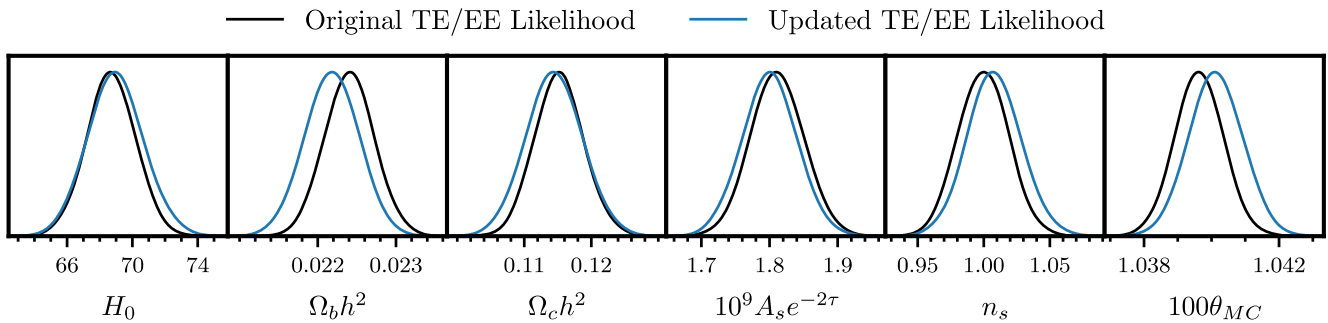


FIG. 13. Marginalized posterior distributions for core  $\Lambda$ CDM and  $\Omega_0$  from the original (black) and updated (blue) SPT-3G 2018 TE=EE likelihood. The posteriors widen slightly; the largest change is a 15% correction to the  $\Omega_0$  uncertainty. The shift to the central values of parameter constraints are less than the size of the new error bars.

## APPENDIX B: BASELINE PRIORS

We present the baseline priors used in the likelihood analysis and the best-fit values of nuisance parameters in  $\Lambda$ CDM in Table VIII.

We briefly present updates made to the galactic dust prior calculation of D21 here. We model the spectral dependence of galactic dust using a modified black-body spectrum and extragalactic foregrounds and the bin width of the cross-spectrum band powers. We conservatively widen the law. The spectra are normalized at 150 GHz and  $1/4$  80. constraints the data provide on the galactic dust amplitudes

We fit combinations of the cross-spectra of the 142, 17, 353, and 545 GHz Planck PR3 half-mission maps [80] calculated on the SPT-3G survey field to the best-fit Planck CMB spectrum plus galactic dust and extragalactic foregrounds. We ensure the resulting constraints on the galactic dust parameters are robust with respect to the modeling of extragalactic foregrounds and the bin width of the cross-spectrum band powers. We conservatively widen the constraints the data provide on the galactic dust amplitudes

TABLE VIII. Overview of nuisance parameters in the SPT-3G 2018 likelihood and baseline priors. Gaussian priors are listed as  $N(\mu; \sigma)$  where  $\mu$  is the mean and  $\sigma$  the standard deviation. Best-fit values for nuisance parameters are given in brackets. All amplitude parameters are in units of  $10^9$ . The best-fit values of all nuisance parameters lie within  $1.2\sigma$  of the central values of their priors. The prior on the optical depth to reionization is not used when including Planck data in the analysis.

Parameter	Prior	Description
<b>General</b>		
$\tau$	$N(0.0540; 0.0074)$	Optical depth to reionization
$100\kappa$	$N(0; 0.045)$	Super-sample lensing convergence
<b>Temperature</b>		
$A_{80}^{\text{cirrus}}$	$N(1.88; 0.48)$	Galactic cirrus amplitude
$\alpha^{\text{cirrus}}$	$N(-2.53; 0.05)$	Galactic cirrus power law index
$\beta^{\text{cirrus}}$	$N(1.48; 0.02)$	Galactic cirrus spectral index
$D_{3000; 95 \times 95}^{\text{Poisson; TT}}$	$N(51.3; 9.4)$	TT Poisson power for $95 \times 95$ GHz
$D_{3000; 95 \times 150}^{\text{Poisson; TT}}$	$N(22.4; 7.1)$	TT Poisson power for $95 \times 150$ GHz
$D_{3000; 95 \times 220}^{\text{Poisson; TT}}$	$N(20.7; 5.9)$	TT Poisson power for $95 \times 220$ GHz
$D_{3000; 150 \times 150}^{\text{Poisson; TT}}$	$N(15.3; 4.1)$	TT Poisson power for $150 \times 150$ GHz
$D_{3000; 150 \times 220}^{\text{Poisson; TT}}$	$N(28.4; 4.2)$	TT Poisson power for $150 \times 220$ GHz
$D_{3000; 220 \times 220}^{\text{Poisson; TT}}$	$N(76.0; 14.9)$	TT Poisson power for $220 \times 220$ GHz
$A_{80}^{\text{CIB-cl.}}$	$N(3.2; 1.8)$	CIB clustering amplitude
$\beta^{\text{CIB-cl.}}$	$N(2.26; 0.38)$	CIB clustering spectral index
$A^{\text{TSZ}}$	$N(3.2; 2.4)$	TSZ amplitude
$\xi$	$N(0.18; 0.33)$	TSZ-CIB correlation
$A^{\text{KSZ}}$	$N(3.7; 4.6)$	KSZ amplitude

(Table continued)

TABLE VIII. (Continued)

Parameter	Prior	Description
<b>Polarization</b>		
$D_{\text{Poisson};\text{EE}}^{3000;95\times95}$	$N(\delta 0.041; 0.012)$	EE Poisson power for $95 \times 95$ GHz
$D_{\text{Poisson};\text{EE}}^{3000;95\times150}$	$N(\delta 0.0180; 0.0054)$	EE Poisson power for $95 \times 150$ GHz
$D_{\text{Poisson};\text{EE}}^{3000;95\times220}$	$N(\delta 0.0157; 0.0047)$	EE Poisson power for $95 \times 220$ GHz
$D_{\text{Poisson};\text{EE}}^{3000;150\times150}$	$N(\delta 0.0115; 0.0034)$	EE Poisson power for $150 \times 150$ GHz
$D_{\text{Poisson};\text{EE}}^{3000;150\times220}$	$N(\delta 0.0190; 0.0057)$	EE Poisson power for $150 \times 220$ GHz
$D_{\text{Poisson};\text{EE}}^{3000;220\times220}$	$N(\delta 0.048; 0.014)$	EE Poisson power for $220 \times 220$ GHz
$A_{80}^{\text{TE}}$	$N(\delta 0.120; 0.051)$	TE amplitude of polarized galactic dust
$\alpha_{\text{TE}}$	$N(\delta -2.42; 0.04)$	TE power law index of polarized galactic dust
$\beta_{\text{TE}}$	$N(\delta 1.51; 0.04)$	TE spectral index of polarized galactic dust
$A_{80}^{\text{EE}}$	$N(\delta 0.05; 0.022)$	EE amplitude of polarized galactic dust
$\alpha_{\text{EE}}$	$N(\delta -2.42; 0.04)$	EE power law index of polarized galactic dust
$\beta_{\text{EE}}$	$N(\delta 1.51; 0.04)$	EE spectral index of polarized galactic dust
<b>Calibration</b>		
$T_{\text{cal}}^{95 \text{ GHz}}$	$N(\delta 1.0; 0.0056)$	Temperature calibration at 95 GHz
$T_{\text{cal}}^{150 \text{ GHz}}$	$N(\delta 1.0; 0.0056)$	Temperature calibration at 150 GHz
$T_{\text{cal}}^{220 \text{ GHz}}$	$N(\delta 1.0; 0.0075)$	Temperature calibration at 220 GHz
$E_{\text{cal}}^{95 \text{ GHz}}$	$N(\delta 1.0; 0.0087)$	Polarization calibration at 95 GHz
$E_{\text{cal}}^{150 \text{ GHz}}$	$N(\delta 1.0; 0.0082)$	Polarization calibration at 150 GHz
$E_{\text{cal}}^{220 \text{ GHz}}$	$N(\delta 1.0; 0.016)$	Polarization calibration at 220 GHz

by a factor of 3 before adopting them as priors in our cosmological analysis. The baseline priors on galactic dust are listed in Table VIII.

### APPENDIX C: MULTIFREQUENCY BAND POWERS

We present the full multifrequency power spectrum measurements in Tables IX–XI below.

TABLE IX. TT multifrequency band power measurements, and associated uncertainties, (both in units of  $\mu\text{K}^2$ ) for a given angular multipole range and the window function-weighted multipole  $l_{\text{eff}}$ .

l Range	$l_{\text{eff}}$	95 $\times$ 95 GHz		95 $\times$ 150 GHz		95 $\times$ 220 GHz		150 $\times$ 150 GHz		150 $\times$ 220 GHz		220 $\times$ 220 GHz	
		$D_b$	$\sigma_b$	$D_b$	$\sigma_b$	$D_b$	$\sigma_b$	$D_b$	$\sigma_b$	$D_b$	$\sigma_b$	$D_b$	$\sigma_b$
750–800	775	2549.3	83.9	2556.1	84.1	2583.5	92.3	2567.7	85.3				
800–850	825	2673.5	79.2	2682.0	79.3	2682.8	87.4	2694.6	80.5				
850–900	874	2191.5	73.7	2185.9	73.9	2185.8	80.9	2187.5	75.1				
900–950	925	1594.4	53.1	1602.2	53.2	1641.3	59.4	1618.7	54.2				
950–1000	974	1215.8	39.5	1211.3	39.6	1213.4	44.6	1211.0	40.4				
1000–1050	1024	1024.5	34.4	1014.3	34.2	1009.6	38.7	1009.8	34.8	1014.1	40.4	1050.0	52.3
1050–1100	1074	1244.8	35.8	1237.7	35.5	1247.4	39.6	1236.6	36.0	1254.6	41.1	1291.8	51.9
1100–1150	1124	1243.4	37.1	1238.0	36.7	1223.3	40.7	1240.4	37.2	1236.7	42.0	1266.1	52.1
1150–1200	1174	1223.5	37.7	1214.2	37.3	1212.3	40.8	1211.2	37.7	1216.1	41.9	1239.0	50.9
1200–1250	1224	940.3	29.0	926.8	28.6	943.7	32.2	921.5	29.1	950.9	33.3	1011.0	42.4
1250–1300	1274	792.3	23.5	780.9	22.9	766.8	26.1	778.6	23.2	776.3	26.9	798.8	35.9
1300–1350	1324	753.0	21.8	744.8	21.3	746.0	24.6	744.1	21.7	757.8	25.4	809.8	33.9
1350–1400	1374	797.3	24.8	786.4	24.2	775.9	26.9	782.8	24.4	783.7	27.6	811.3	35.1

(Table continued)

TABLE IX. (Continued)

l Range	l <sub>eff</sub>	95 × 95 GHz		95 × 150 GHz		95 × 220 GHz		150 × 150 GHz		150 × 220 GHz		220 × 220 GHz	
		D <sub>b</sub>	σ <sub>b</sub>										
1400–1450	1424	828.7	24.7	818.0	24.1	819.6	26.8	818.0	24.4	833.5	27.6	881.0	34.9
1450–1500	1474	774.5	22.4	766.8	21.7	772.6	24.5	766.1	22.1	783.2	25.2	825.6	32.6
1500–1550	1524	653.0	19.6	643.3	19.0	656.6	21.5	642.3	19.2	666.9	22.0	724.2	29.2
1550–1600	1574	517.8	14.8	501.6	14.1	497.6	16.7	495.4	14.2	503.3	17.2	550.5	24.9
1600–1650	1624	436.4	13.7	421.1	13.1	412.1	15.5	416.6	13.3	421.8	16.0	467.8	23.6
1650–1700	1674	426.5	11.9	412.9	11.3	411.4	14.2	407.7	11.6	420.2	14.7	473.6	22.8
1700–1750	1724	424.4	13.2	413.2	12.6	412.0	15.3	411.3	12.9	422.7	15.8	484.8	23.6
1750–1800	1775	408.9	12.0	395.3	11.4	404.6	14.2	394.3	11.7	417.0	14.7	477.5	22.5
1800–1850	1824	390.5	11.0	372.1	10.3	362.0	12.9	365.4	10.5	370.0	13.3	415.1	21.0
1850–1900	1874	309.6	9.9	288.4	9.1	283.1	11.7	280.1	9.3	291.1	11.9	356.4	19.6
1900–1950	1925	264.0	8.7	250.3	7.9	253.7	10.4	247.9	8.0	265.5	10.5	317.3	18.4
1950–2000	1974	279.4	8.5	256.6	7.6	241.7	10.1	248.9	7.7	253.0	10.2	319.1	18.2
2000–2100	2051	264.0	4.5	245.8	4.0	242.7	5.4	241.3	4.1	253.9	5.5	317.3	10.0
2100–2200	2152	215.1	4.1	192.8	3.6	189.5	5.0	186.1	3.7	198.8	5.0	251.4	9.8
2200–2300	2250	170.0	3.4	146.2	2.7	145.3	4.3	141.5	2.8	157.5	4.2	240.8	9.3
2300–2400	2350	158.6	3.2	138.8	2.5	132.4	4.2	135.5	2.5	155.4	3.9	230.5	9.3
2400–2500	2451	142.6	3.0	117.9	2.3	120.5	3.9	111.4	2.2	132.1	3.6	216.0	9.2
2500–2600	2550	128.0	2.9	98.7	2.1	93.8	3.8	91.8	2.0	107.7	3.4	178.6	9.3
2600–2700	2649	122.7	2.9	91.6	1.9	84.8	3.8	85.7	1.9	106.1	3.2	191.6	9.4
2700–2800	2750	118.5	2.9	85.1	1.9	75.1	3.9	74.6	1.7	87.9	3.2	183.0	9.7
2800–2900	2850	107.3	2.9	74.8	1.8	71.8	3.9	64.9	1.6	89.7	3.1	207.5	10.1
2900–3000	2947	109.5	3.1	70.5	1.8	59.8	4.1	58.4	1.6	75.6	3.1	154.3	10.5

TABLE X. TE multifrequency band power measurements, and associated uncertainties, (both in units of  $\mu\text{K}^2$ ) for a given angular multipole range and the window function-weighted multipole. The data have been minorly updated from D21.

l Range	l <sub>eff</sub>	95 × 95 GHz		95 × 150 GHz		95 × 220 GHz		150 × 150 GHz		150 × 220 GHz		220 × 220 GHz	
		D <sub>b</sub>	σ <sub>b</sub>										
300–350	326	88.7	12.0	93.3	12.2	99.7	13.9	101.1	12.7	110.2	14.4	113.2	20.3
350–400	375	43.8	8.8	42.5	8.7	36.6	10.7	42.7	9.2	40.7	11.3	39.9	17.2
400–450	425	-44.9	7.6	-45.6	7.3	-43.0	9.2	-47.8	7.5	-47.0	9.5	-43.2	15.0
450–500	475	-69.1	6.7	-69.0	6.3	-64.9	7.9	-70.0	6.4	-64.4	8.0	-53.0	13.2
500–550	525	-34.1	5.5	-34.7	5.0	-48.2	6.7	-34.8	5.2	-46.6	6.7	-57.9	12.1
550–600	575	11.9	6.2	11.3	5.9	15.2	7.4	10.5	6.1	15.5	7.5	20.7	12.3
600–650	625	24.2	7.0	23.9	6.7	21.5	8.2	24.5	7.0	23.0	8.3	21.3	12.7
650–700	674	-63.6	7.7	-63.4	7.4	-58.0	8.7	-63.1	7.5	-59.1	8.8	-59.7	12.9
700–750	725	-119.9	7.3	-121.2	6.9	-114.0	8.3	-122.8	7.0	-115.7	8.3	-104.7	12.6
750–800	774	-121.7	7.3	-120.7	6.7	-124.1	8.3	-121.4	6.8	-126.0	8.2	-124.1	12.8
800–850	824	-52.8	5.6	-50.6	4.8	-43.2	6.8	-48.6	5.0	-39.9	6.7	-25.5	12.0
850–900	874	41.2	5.8	38.5	5.1	38.5	6.9	36.7	5.3	37.2	6.9	36.6	11.8
900–950	924	54.7	5.5	56.1	4.9	58.9	6.6	56.9	5.1	61.3	6.6	70.1	11.2
950–1000	974	12.5	5.3	13.1	4.9	14.4	6.3	13.9	5.0	13.7	6.3	17.9	10.6
1000–1050	1024	-52.2	5.6	-51.9	5.2	-55.4	6.5	-51.8	5.4	-55.7	6.5	-56.4	10.5
1050–1100	1074	-75.8	5.3	-74.7	4.7	-71.9	6.2	-73.7	4.9	-72.0	6.1	-69.8	10.4
1100–1150	1124	-48.4	4.6	-52.8	3.9	-58.4	5.6	-55.9	4.1	-60.2	5.5	-65.8	10.1
1150–1200	1174	-9.7	4.2	-10.1	3.4	-6.9	5.2	-10.8	3.6	-7.1	5.1	-1.9	9.9
1200–1250	1224	4.9	4.1	4.3	3.4	4.2	5.1	4.3	3.6	4.3	5.0	8.3	9.7
1250–1300	1274	-15.4	4.1	-15.8	3.4	-17.2	5.1	-16.1	3.6	-16.7	4.9	-16.3	9.5
1300–1350	1324	-47.3	4.2	-48.2	3.5	-43.6	5.1	-49.1	3.6	-42.8	5.0	-39.5	9.5
1350–1400	1374	-62.0	4.3	-62.0	3.5	-55.3	5.3	-63.0	3.7	-56.7	5.1	-47.3	9.9
1400–1450	1424	-41.2	4.1	-41.9	3.1	-41.2	5.2	-42.9	3.3	-41.0	5.0	-30.7	10.1

(Table continued)

TABLE X. (Continued)

l Range	l <sub>eff</sub>	95 × 95 GHz		95 × 150 GHz		95 × 220 GHz		150 × 150 GHz		150 × 220 GHz		220 × 220 GHz	
		D <sub>b</sub>	σ <sub>b</sub>										
1450–1500	1474	−10.9	3.9	−11.8	2.8	−8.6	5.0	−13.0	3.0	−9.9	4.7	−4.2	10.0
1500–1550	1524	8.5	3.6	9.1	2.6	4.8	4.7	10.2	2.8	5.9	4.5	−7.3	9.7
1550–1600	1574	−3.8	3.5	−0.8	2.6	−4.2	4.5	1.1	2.8	0.3	4.3	−5.1	9.4
1600–1650	1624	−13.9	3.4	−15.4	2.6	−15.7	4.4	−14.5	2.7	−13.3	4.1	−8.0	9.3
1650–1700	1674	−31.1	3.3	−32.0	2.4	−32.4	4.3	−33.1	2.5	−31.7	4.0	−32.9	9.4
1700–1750	1724	−22.0	3.4	−24.0	2.3	−25.9	4.4	−26.0	2.5	−26.7	4.1	−25.0	9.7
1750–1800	1775	−15.8	3.3	−15.2	2.2	−17.6	4.4	−14.7	2.4	−17.4	4.0	−21.4	9.9
1800–1850	1824	−14.2	3.2	−10.0	2.1	−7.1	4.3	−8.4	2.2	−7.3	3.9	3.4	9.8
1850–1900	1874	−3.9	3.1	−3.3	2.0	−5.1	4.1	−3.4	2.2	−3.3	3.8	−12.6	9.7
1900–1950	1924	−11.9	3.0	−11.2	2.0	−10.8	4.1	−11.3	2.1	−10.9	3.7	−13.9	9.7
1950–2000	1975	−15.1	3.1	−16.4	2.0	−17.8	4.1	−16.4	2.1	−17.2	3.7	−18.6	10.0
2000–2100	2050	−16.1	1.7	−14.2	1.0	−14.6	2.3	−13.7	1.1	−13.9	2.0	−17.7	5.6
2100–2200	2150	−5.4	1.6	−4.8	1.0	−9.1	2.3	−4.3	1.1	−5.8	2.0	3.5	5.9
2200–2300	2250	−7.7	1.6	−6.4	0.9	−3.9	2.3	−5.0	1.0	−3.6	1.9	−8.8	6.1
2300–2400	2350	−8.9	1.7	−8.8	0.9	−10.5	2.4	−9.3	1.0	−10.5	1.9	−19.6	6.4
2400–2500	2450	−7.5	1.7	−4.7	0.9	−5.7	2.4	−2.3	0.9	−0.4	1.9	0.3	6.7
2500–2600	2550	−0.9	1.7	−4.2	0.9	−4.0	2.5	−3.6	0.9	−5.1	1.9	−14.1	7.0
2600–2700	2649	−4.9	1.8	−3.3	0.9	−6.6	2.6	−3.2	0.9	−3.7	1.9	−2.4	7.4
2700–2800	2749	1.5	1.9	−2.1	1.0	5.2	2.8	−3.8	0.9	1.9	2.0	16.4	7.9
2800–2900	2849	2.5	2.1	0.2	1.0	−0.2	3.0	−0.7	1.0	−5.4	2.1	−3.9	8.4
2900–3000	2946	−7.8	2.3	−2.3	1.1	−5.5	3.2	−2.2	1.0	0.8	2.2	16.9	9.0

TABLE XI. EE multifrequency band power measurements, and associated uncertainties, (both in units of  $\mu\text{K}^2$ ) for a given angular multipole range and the window function-weighted multipole. The data have been minorly updated from D21.

l Range	l <sub>eff</sub>	95 × 95 GHz		95 × 150 GHz		95 × 220 GHz		150 × 150 GHz		150 × 220 GHz		220 × 220 GHz	
		D <sub>b</sub>	σ <sub>b</sub>										
300–350	325	13.1	1.1	12.7	1.1	11.9	1.3	13.0	1.1	12.5	1.3	11.7	2.0
350–400	375	19.7	1.3	20.4	1.3	18.7	1.5	20.9	1.3	19.5	1.5	17.5	2.3
400–450	425	19.0	1.2	18.7	1.1	17.7	1.3	18.9	1.1	18.1	1.3	17.2	2.1
450–500	475	11.2	0.7	11.9	0.7	11.0	0.9	12.4	0.7	10.9	0.9	9.2	1.7
500–550	524	7.1	0.5	7.2	0.4	7.5	0.6	6.9	0.4	8.1	0.6	9.1	1.5
550–600	575	11.1	0.7	11.2	0.6	12.1	0.9	11.7	0.7	11.6	0.9	11.2	1.9
600–650	624	29.1	1.3	29.3	1.2	28.7	1.5	29.8	1.2	29.2	1.4	33.3	2.5
650–700	674	39.0	1.5	38.9	1.3	38.9	1.7	38.5	1.4	39.0	1.7	39.7	2.9
700–750	725	33.7	1.4	34.2	1.3	32.6	1.7	34.7	1.3	33.5	1.6	31.5	2.9
750–800	774	21.2	1.1	20.7	0.9	21.7	1.3	20.2	0.9	20.9	1.2	22.2	2.7
800–850	824	13.2	0.8	13.3	0.6	13.0	1.0	13.6	0.6	13.1	0.9	13.2	2.5
850–900	874	16.9	0.9	17.1	0.7	17.6	1.2	16.9	0.8	17.4	1.1	18.6	2.9
900–950	924	31.8	1.3	31.3	1.1	30.3	1.6	31.3	1.1	31.7	1.5	28.8	3.4
950–1000	974	41.3	1.6	40.2	1.4	40.1	2.0	40.3	1.4	39.1	1.9	35.8	3.9
1000–1050	1024	39.4	1.6	38.2	1.3	38.7	2.0	38.1	1.4	36.6	1.9	39.6	4.1
1050–1100	1075	26.1	1.3	26.1	1.0	24.6	1.7	26.1	1.1	24.8	1.5	19.8	3.9
1100–1150	1124	15.5	1.0	15.1	0.7	14.4	1.4	14.8	0.7	13.6	1.2	10.4	3.8
1150–1200	1174	13.1	1.0	12.2	0.7	10.7	1.4	12.5	0.7	11.8	1.2	12.2	4.0
1200–1250	1224	20.6	1.3	21.7	0.9	23.6	1.7	21.9	1.0	21.9	1.5	17.5	4.5
1250–1300	1275	29.9	1.5	29.0	1.1	28.1	2.0	29.3	1.2	26.4	1.8	26.1	5.0
1300–1350	1325	31.2	1.6	30.7	1.1	28.1	2.1	31.8	1.2	27.9	1.9	23.7	5.4
1350–1400	1374	24.1	1.4	22.3	1.0	21.8	2.0	22.0	1.0	24.5	1.7	38.9	5.6
1400–1450	1424	14.2	1.3	12.9	0.8	11.7	1.9	12.4	0.8	11.1	1.5	5.3	5.7
1450–1500	1474	10.9	1.3	10.1	0.7	11.3	2.0	10.3	0.8	13.2	1.5	18.7	6.1

(Table continued)

TABLE XI. (Continued)

l Range	l <sub>eff</sub>	95 × 95 GHz		95 × 150 GHz		95 × 220 GHz		150 × 150 GHz		150 × 220 GHz		220 × 220 GHz	
		D <sub>b</sub>	σ <sub>b</sub>										
1500–1550	1524	15.0	1.4	15.3	0.8	12.4	2.2	14.0	0.9	10.9	1.7	7.8	6.5
1550–1600	1574	22.1	1.6	20.8	1.0	21.8	2.4	20.9	1.0	23.7	2.0	23.1	7.0
1600–1650	1624	17.6	1.7	19.9	1.0	20.2	2.6	20.5	1.1	21.3	2.1	23.3	7.4
1650–1700	1674	19.2	1.7	18.3	1.0	14.4	2.6	17.9	1.0	18.5	2.0	12.6	7.7
1700–1750	1724	7.4	1.7	10.1	0.9	10.7	2.6	10.4	0.9	13.9	1.9	0.3	8.1
1750–1800	1775	10.1	1.7	8.7	0.9	11.1	2.7	8.4	0.9	7.9	1.9	14.5	8.6
1800–1850	1825	8.3	1.8	9.0	0.9	5.7	2.9	9.5	0.9	5.3	2.1	-0.4	9.1
1850–1900	1874	9.7	2.0	9.7	1.0	9.5	3.1	9.7	1.0	12.8	2.3	13.8	9.7
1900–1950	1924	12.7	2.1	12.8	1.1	17.9	3.3	11.8	1.1	7.6	2.4	0.6	10.3
1950–2000	1975	12.4	2.2	10.1	1.1	8.8	3.4	11.3	1.1	13.7	2.5	6.0	10.9
2000–2100	2049	6.7	1.2	6.2	0.6	7.7	2.0	6.3	0.6	6.1	1.4	4.7	6.4
2100–2200	2148	5.3	1.3	5.5	0.7	1.0	2.2	5.3	0.6	5.2	1.5	9.1	7.2
2200–2300	2249	7.4	1.5	7.6	0.7	6.6	2.5	5.9	0.7	7.0	1.7	8.6	8.1
2300–2400	2349	1.2	1.7	2.6	0.8	4.1	2.8	4.8	0.7	1.0	1.8	13.0	8.8
2400–2500	2449	6.6	1.9	4.0	0.9	5.2	3.0	2.6	0.8	5.1	1.9	-0.9	9.7
2500–2600	2549	2.7	2.1	2.5	0.9	0.4	3.3	2.6	0.9	3.0	2.1	-2.5	10.6
2600–2700	2649	5.8	2.3	0.5	1.0	0.0	3.7	2.3	0.9	2.2	2.3	10.3	11.6
2700–2800	2749	-0.8	2.6	0.8	1.2	9.1	4.1	2.0	1.0	3.5	2.6	-5.3	12.8
2800–2900	2849	0.9	3.0	3.1	1.3	4.6	4.6	0.5	1.2	-3.2	2.9	-6.2	14.0
2900–3000	2946	-2.0	3.4	-2.6	1.5	-7.2	5.1	1.0	1.3	7.3	3.2	-4.2	15.5

## APPENDIX D: DIFFERENCE SPECTRA

We follow Planck Collaboration et al. [41] and form difference spectra,  $\Delta^{1/4} \hat{D}^{VU} - \hat{D}^{KT}$ , where  $\hat{D}^{VU}$  are foreground-subtracted multifrequency band powers. The covariance of a difference spectrum is  $\Delta^{VU;KT} \Delta^{VU;KT} A^T$ , where  $\Delta^{VU;KT}$  is the  $2 \times 2$  matrix of the relevant covariance blocks and  $A^{1/4} \delta l; -l b$ .

We show the TT, TE, and EE difference spectra in Figs. 14–16, respectively. While we observe no significant features, such as slopes, constant offsets, or signal leakage, the TT difference spectra show a dip at  $l \approx 2350$ . This is caused by a bifurcation of the multifrequency spectra over a region of  $\Delta l \approx 300$  width, with higher frequencies seeing a stronger signal. This feature is not present in the polarization spectra. It is not clear what is causing this bifurcation; for unmodeled foreground contamination we expect to see a slope in the difference spectra, rather than a well-localized feature. Ultimately, this feature is not statistically significant: comparing the 45 difference spectra to zero using a  $\chi^2$  statistic, the lowest PTE value is 5% (150 × 220 GHz – 95 × 95 GHz TT). We conclude that the difference spectra are consistent with zero and take this as further evidence that the multifrequency band powers are consistent with measuring the same underlying signal.

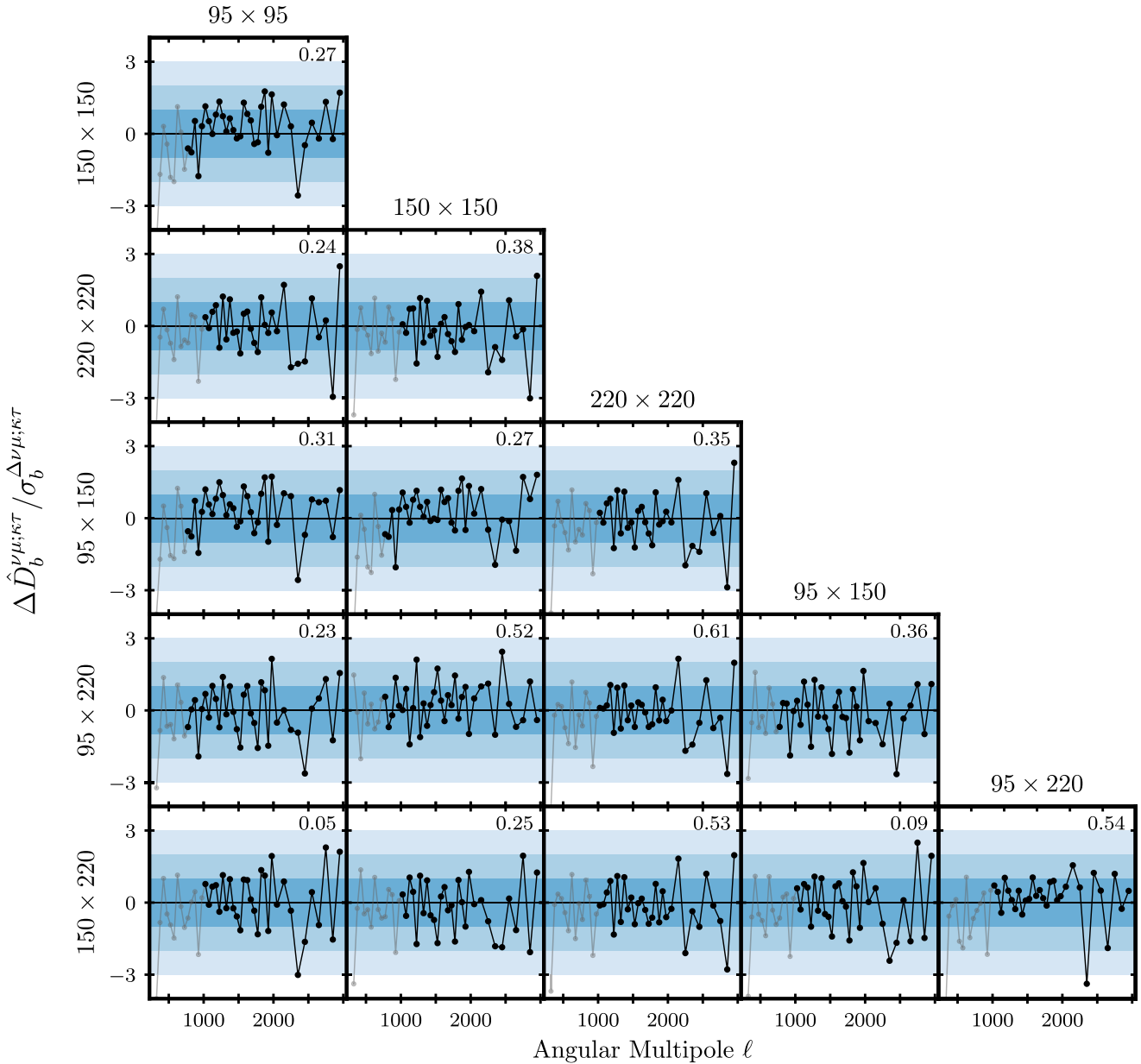


FIG. 14. Relative TT difference spectra as indicated by the row and column labels, i.e. difference  $\hat{\Delta}D_b^{\nu\mu;\kappa\tau}$  specified by the square root of the associated covariance,  $\sigma_b^{\Delta\nu\mu;\kappa\tau}$ . The blue shading indicates the range of  $1 - 3\sigma$  fluctuations, while gray indicates data excluded in the analysis. We conservatively exclude all TT data at  $\ell < 750$ . This is motivated by the shape of the transfer function, which slowly rises and plateaus at  $\ell \approx 750$ ; the common-mode filter removes TT power on large and intermediate angular scales. We further exclude 150 × 220 GHz and 220 × 220 GHz TT spectra at  $\ell < 1000$ , based on our model for correlated atmospheric noise. The PTE values are indicated in the top right corner of each panel. All PTE values are in the 95th percentile and the multifrequency spectra are in good agreement with one another.

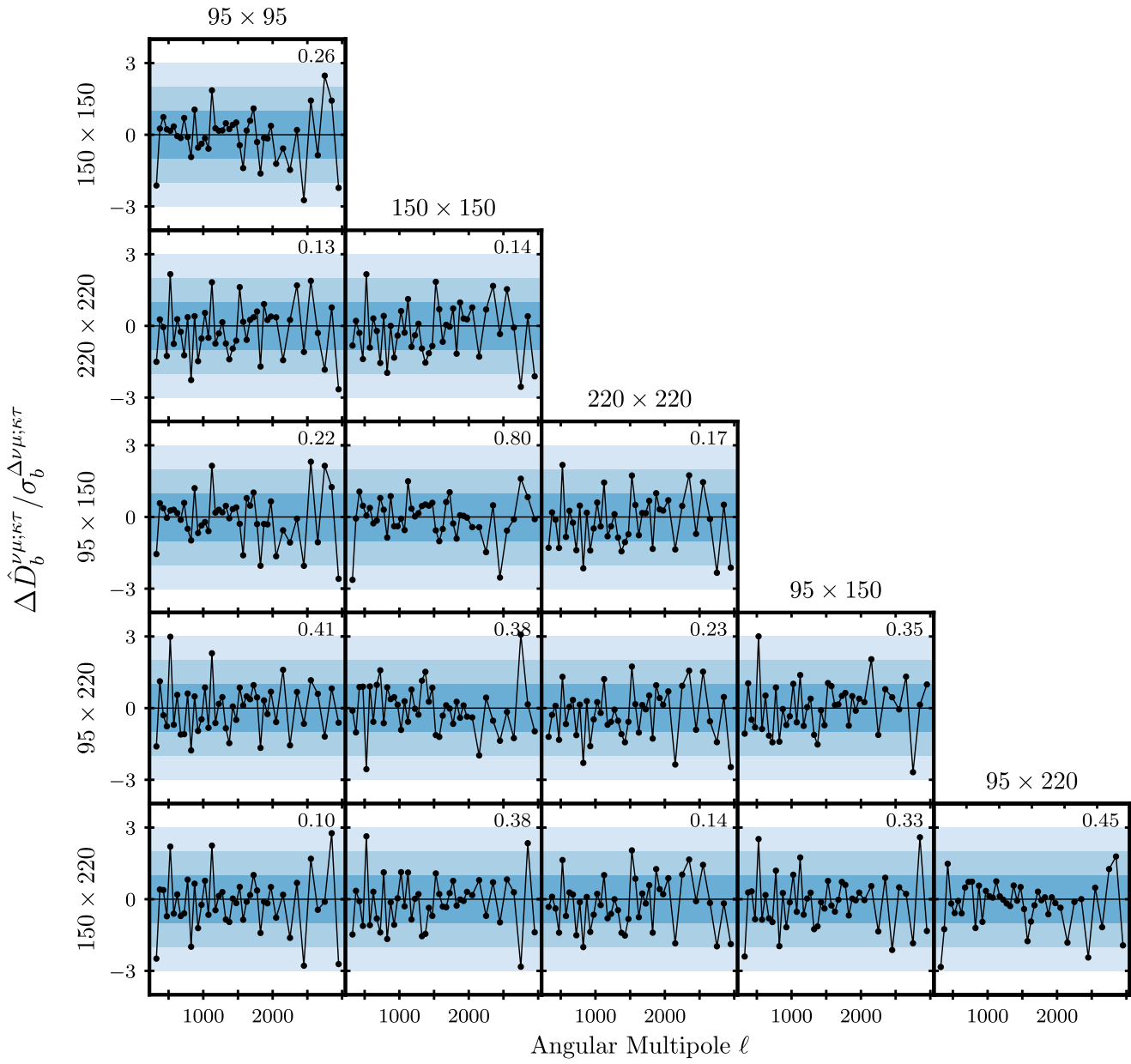


FIG. 15. Relative TE difference spectra as indicated by the row and column labels, i.e. difference  $\hat{\Delta}D_b^{\mu:\kappa\tau}$  specified by the square root of the associated covariance  $\Delta\nu^{\mu:\kappa\tau}$ . The blue shading indicates the range of  $1 - 3\sigma$  fluctuations and PTE values are given in the top right corner of each panel. All PTE values are in the 95th percentile and the multifrequency spectra are in good agreement with one another.

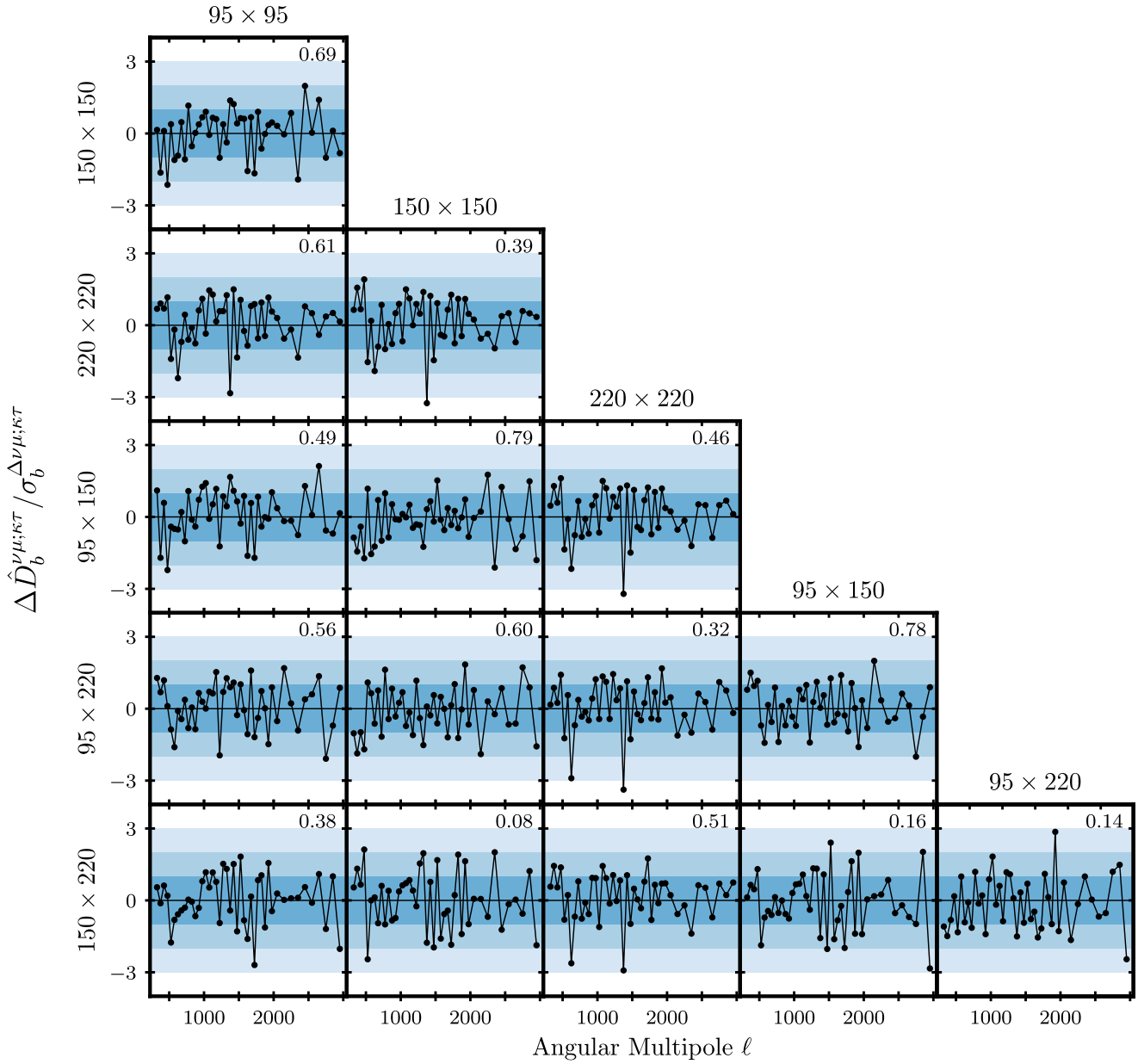


FIG. 16. Relative EE difference spectra as indicated by the row and column labels, i.e. difference  $\hat{D}_b^{\nu\mu;\kappa\tau}$  divided by the square root of the associated covariance,  $\sigma_b^{\Delta\nu\mu;\kappa\tau}$ . The blue shading indicates the range of  $1 - 3\sigma$  fluctuations. The multifrequency spectra are in good agreement with one another, as evidenced by the PTE values (given in the top right corner of each panel) which all lie in the 95th percentile.

## APPENDIX E: MULTIFREQUENCY RESIDUALS

We show the residuals of the SPT-3G 2018 TT=TE=EE multifrequency band powers to the best-fit  $\Lambda$ CDM model in Fig. 17.

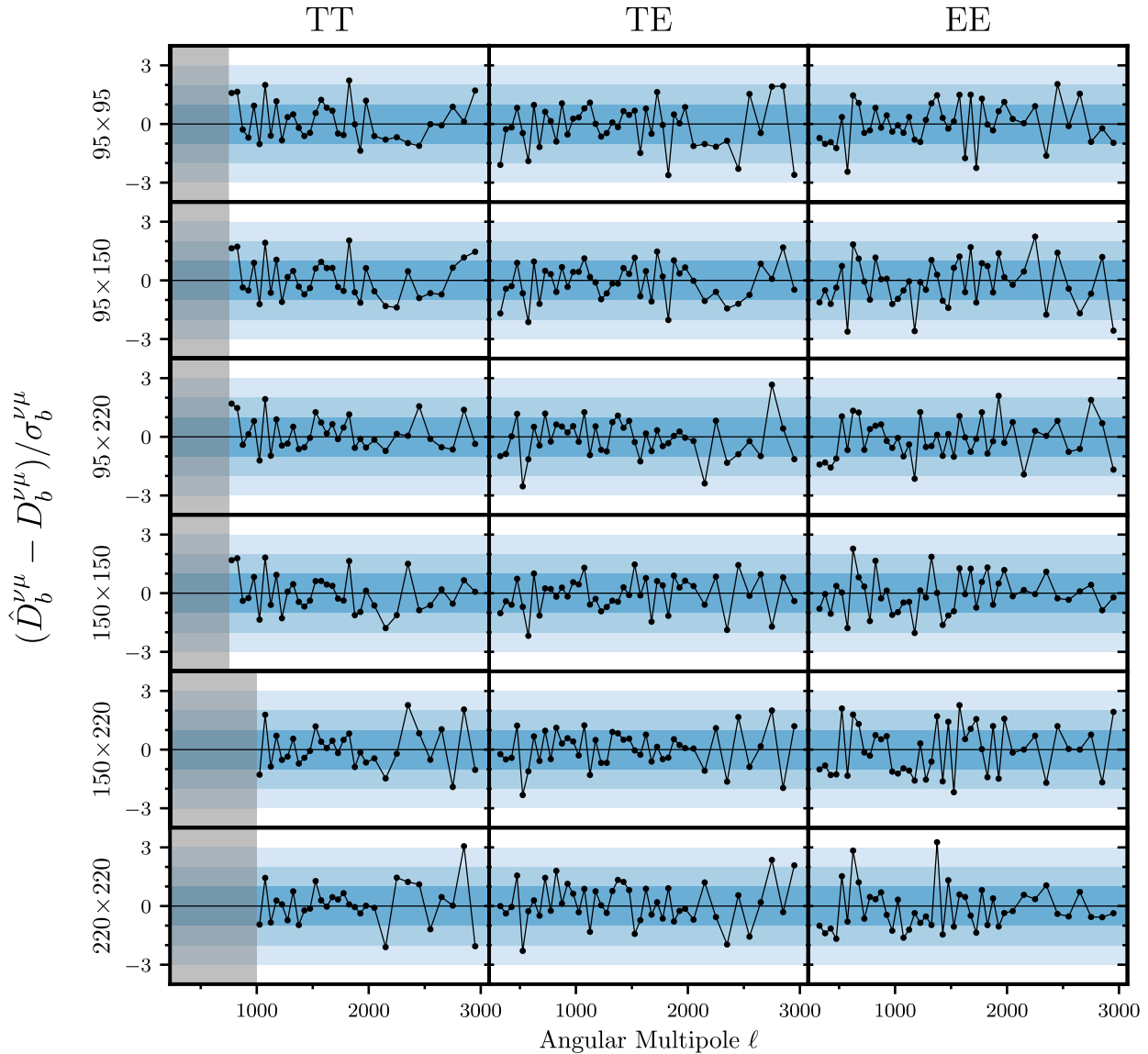


FIG. 17. Relative residuals of the SPT-3G 2018 TT=TE=EE multifrequency band powers to the best-fit  $\Lambda$ CDM model, i.e. difference between the SPT-3G data and the model prediction scaled by the error bar of the band powers measurement. The blue shading indicates the range of  $1 - 3\sigma$  fluctuations. Note that the SPT-3G band powers are correlated by up to 40% for neighboring bins. The residuals are consistent with zero and the standard model provides a good fit to the data.

[1] N. Aghanim, Y. Akrami et al. (Planck Collaboration), Planck 2018 results. VI. Cosmological parameters, *Astron. Astrophys.* **641**, A6 (2020).

[2] D. Dutcher, L. Balkenhol, P. A. R. Ade et al., Measurements of the E-mode polarization and temperature-E-mode correlation of the CMB from SPT-3G 2018 data, *Phys. Rev. D* **104**, 022003 (2021).

[3] L. Balkenhol, D. Dutcher, P. A. R. Ade et al., Constraints on  $\Lambda$ CDM extensions from the SPT-3G 2018 E E and T E power spectra, *Phys. Rev. D* **104**, 083509 (2021).

[4] S. K. Choi, M. Hasselfield, S.-P. P. Ho et al., The Atacama Cosmology Telescope: A measurement of the cosmic microwave background power spectra at 98 and 150 GHz, *J. Cosmol. Astropart. Phys.* **12** (2020) 045.

[5] S. Aiola, E. Calabrese, L. Maurin et al., The Atacama Cosmology Telescope: DR4 maps and cosmological parameters, *J. Cosmol. Astropart. Phys.* **12** (2020) 047.

[6] J. E. Carlstrom, P. A. R. Ade, K. A. Aird et al., The 10 m south pole telescope, *Publ. Astron. Soc. Pac.* **123**, 568 (2011).

[7] A. Kosowsky, The Atacama Cosmology Telescope, in Proceedings of the Workshop on “The Cosmic Microwave Background and its Polarization”, New Astronomy Reviews, edited by S. Hanany and K. A. Olive (Elsevier, New York, 2003).

[8] Z. D. Kermish, P. Ade, A. Anthony et al., The POLAR-BEAR experiment, in Society of Photo-Optical Instrumentation Engineers (SPIE) Conference Series, Millimeter, Submillimeter, and Far-Infrared Detectors and Instrumentation for Astronomy VI, edited by W. S. Holland and J. Zmuidzinas (2012), Vol. 8452, p. 84521C, [10.1117/12.926354](https://doi.org/10.1117/12.926354).

[9] B. G. Keating, P. A. R. Ade, J. J. Bock, E. Hivon, W. L. Holzapfel, A. E. Lange, H. Nguyen, and K. Yoon, BICEP: A large angular scale CMB polarimeter, in Polarimetry in Astronomy, Proceedings of the SPIE Vol 4843, edited by Silvano Fineschi (SPIE, Waikoloa, Hawaii, USA, 2003), pp. 284–295.

[10] Z. Staniszewski, R. W. Aikin, M. Amiri et al., The Keck array: A multi camera CMB polarimeter at the south pole, *J. Low Temp. Phys.* **167**, 827 (2012).

[11] N. Aghanim, Y. Akrami et al. (Planck Collaboration), Planck 2018 results. V. CMB power spectra and likelihoods, *Astron. Astrophys.* **641**, A5 (2020).

[12] S. Galli, K. Benabed, F. Bouchet, J.-F. Cardoso, F. Elsner, E. Hivon, A. Mangilli, S. Prunet, and B. Wandelt, CMB polarization can constrain cosmology better than CMB temperature, *Phys. Rev. D* **90**, 063504 (2014).

[13] C. L. Reichardt, P. A. R. Ade, J. J. Bock et al., High-resolution CMB power spectrum from the complete ACBAR data set, *Astrophys. J.* **694**, 1200 (2009).

[14] S. Das, T. A. Marriage, P. A. R. Ade et al., The Atacama Cosmology Telescope: A measurement of the cosmic microwave background power spectrum at 148 and 218 GHz from the 2008 southern survey, *Astrophys. J.* **729**, 62 (2011).

[15] C. L. Bennett, D. Larson, J. L. Weiland et al., Nine-year Wilkinson microwave anisotropy probe (WMAP) observations: Final maps and results, *Astrophys. J. Suppl. Ser.* **208**, 20 (2013).

[16] K. T. Story, C. L. Reichardt, Z. Hou et al., A measurement of the cosmic microwave background damping tail from the 2500-square-degree SPT-SZ survey, *Astrophys. J.* **779**, 86 (2013).

[17] S. Galli, L. Pogosian, K. Jedamzik, and L. Balkenhol, Consistency of Planck, ACT, and SPT constraints on magnetically assisted recombination and forecasts for future experiments, *Phys. Rev. D* **105**, 023513 (2022).

[18] B. A. Benson, P. A. R. Ade, Z. Ahmed et al., SPT-3G: A next-generation cosmic microwave background polarization experiment on the south pole telescope, in Proceedings of the SPIE Millimeter, Submillimeter, and Far-Infrared Detectors and Instrumentation for Astronomy VII (2014), Vol. 9153, p. 91531P, [10.1117/12.2057305](https://doi.org/10.1117/12.2057305).

[19] J. A. Sobrin, A. J. Anderson, A. N. Bender et al., The design and integrated performance of SPT-3G, *Astrophys. J. Suppl. Ser.* **258**, 42 (2022).

[20] E. Hivon, K. M. Górski, C. B. Netterfield, B. P. Crill, S. Prunet, and F. Hansen, MASTER of the cosmic microwave background anisotropy power spectrum: A fast method for statistical analysis of large and complex cosmic microwave background data sets, *Astrophys. J.* **567**, 2 (2002).

[21] A. Lewis and S. Bridle, Cosmological parameters from CMB and other data: A Monte Carlo approach, *Phys. Rev. D* **66**, 103511 (2002).

[22] A. Lewis, A. Challinor, and A. Lasenby, Efficient computation of cosmic microwave background anisotropies in closed Friedmann-Robertson-Walker models, *Astrophys. J.* **538**, 473 (2000).

[23] A. Spurio Mancini, D. Piras, J. Alsing, B. Joachimi, and M. P. Hobson, COSMOPOWER: Emulating cosmological power spectra for accelerated Bayesian inference from next-generation surveys, *Mon. Not. R. Astron. Soc.* **511**, 1771 (2022).

[24] W. Hu and N. Sugiyama, Small-scale cosmological perturbations: An analytic approach, *Astrophys. J.* **471**, 542 (1996).

[25] W. A. Fendt and B. D. Wandelt, Pico: Parameters for the impatient cosmologist, *Astrophys. J.* **654**, 2 (2007).

[26] D. Blas, J. Lesgourgues, and T. Tram, The cosmic linear anisotropy solving system (CLASS). Part II: Approximation schemes, *J. Cosmol. Astropart. Phys.* **07** (2011) 034.

[27] J. C. Hill, E. Calabrese, S. Aiola et al., Atacama Cosmology Telescope: Constraints on pre-recombination early dark energy, *Phys. Rev. D* **105**, 123536 (2022).

[28] D. Jeong, J. Chluba, L. Dai, M. Kamionkowski, and X. Wang, Effect of aberration on partial-sky measurements of the cosmic microwave background temperature power spectrum, *Phys. Rev. D* **89**, 023003 (2014).

[29] A. Manzotti, W. Hu, and A. Benoit-Lévy, Super-sample CMB lensing, *Phys. Rev. D* **90**, 023003 (2014).

[30] C. L. Reichardt, S. Patil, P. A. R. Ade et al., An improved Measurement of the secondary cosmic microwave background anisotropies from the SPT-SZ + SPTpol surveys, *Astrophys. J.* **908**, 199 (2021).

[31] E. M. George, C. L. Reichardt, K. A. Aird et al., A measurement of secondary cosmic microwave background anisotropies from the 2500-square-degree SPT-SZ survey, *Astrophys. J.* **799**, 177 (2015).

[32] J. Dunkley, E. Calabrese, J. Sievers et al., The Atacama Cosmology Telescope Likelihood for small-scale CMB data, *J. Cosmol. Astropart. Phys.* 07 (2013) 025.

[33] G. De Zotti, R. Ricci, D. Mesa, L. Silva, P. Mazzotta, L. Toffolatti, and J. González-Nuevo, Predictions for high-frequency radio surveys of extragalactic sources, *Astron. Astrophys.* 431, 893 (2005).

[34] D. J. Fixsen, The temperature of the cosmic microwave background, *Astrophys. J.* 707, 916 (2009).

[35] G. E. Addison, J. Dunkley, A. Hajian et al., Power-law template for infrared point-source clustering, *Astrophys. J.* 752, 120 (2012).

[36] L. D. Shaw, D. Nagai, S. Bhattacharya, and E. T. Lau, Impact of cluster physics on the Sunyaev-Zel'dovich power spectrum, *Astrophys. J.* 725, 1452 (2010).

[37] L. D. Shaw, D. H. Rudd, and D. Nagai, Deconstructing the kinetic SZ power spectrum, *Astrophys. J.* 756, 15 (2012).

[38] O. Zahn, C. L. Reichardt, L. Shaw et al., Cosmic microwave background constraints on the duration and timing of reionization from the south pole telescope, *Astrophys. J.* 756, 65 (2012).

[39] P. A. R. Ade, N. Aghanim, C. Armitage-Caplan, M. Arnaud, M. Ashdown, F. Atrio-Barandela, J. Aumont, C. Baccigalupi, A. J. Banday et al. (Planck Collaboration), Planck 2013 results. XV. CMB power spectra and likelihood, *Astron. Astrophys.* 571, A15 (2014).

[40] O. J. Dunn, Multiple Comparisons Among Means, American Statistical Association (Taylor & Francis, Abingdon, UK, 1961), p. 52.

[41] N. Aghanim, M. Arnaud, M. Ashdown, J. Aumont, C. Baccigalupi, A. J. Banday, R. B. Barreiro, J. G. Bartlett, N. Bartolo et al. (Planck Collaboration), Planck 2015 results. XI. CMB power spectra, likelihoods, and robustness of parameters, *Astron. Astrophys.* 594, A11 (2016).

[42] L. M. Mocanu, T. M. Crawford, K. Aylor et al., Consistency of cosmic microwave background temperature measurements in three frequency bands in the 2500-square-degree SPT-SZ survey, *J. Cosmol. Astropart. Phys.* 07 (2019) 038.

[43] S. Gratton and A. Challinor, Understanding parameter differences between analyses employing nested data subsets, *Mon. Not. R. Astron. Soc.* 499, 3410 (2020).

[44] U. Natale, L. Pagano, M. Lattanzi, M. Migliaccio, L. P. Colombo, A. Gruppuso, P. Natoli, and G. Polenta, A novel CMB polarization likelihood package for large angular scales built from combined WMAP and Planck LFI legacy maps, *Astron. Astrophys.* 644, A32 (2020).

[45] J. W. Henning, J. T. Sayre, C. L. Reichardt et al., Measurements of the temperature and E-mode polarization of the CMB from 500 square degrees of SPTpol data, *Astrophys. J.* 852, 97 (2018).

[46] S. Adachi, M. A. O. Aguilar Faúndez, K. Arnold et al., A measurement of the CMB E-mode angular power spectrum at subdegree scales from 670 square degrees of POLAR-BEAR data, *Astrophys. J.* 904, 65 (2020).

[47] A. G. Riess, W. Yuan, L. M. Macri et al., A comprehensive measurement of the local value of the Hubble constant with  $1 \text{ km s}^{-1} \text{ Mpc}^{-1}$  uncertainty from the Hubble space telescope and the SH0ES team, *Astrophys. J. Lett.* 934, L7 (2022).

[48] W. L. Freedman, B. F. Madore, D. Hatt, T. J. Hoyt, I.-S. Jang, R. L. Beaton, C. R. Burns, M. G. Lee, A. J. Monson, J. R. Neeley, M. M. Phillips, J. A. Rich, and M. Seibert, The Carnegie-Chicago Hubble program VIII. An independent determination of the Hubble constant based on the tip of the red giant branch, *Astrophys. J.* 882, 34 (2019).

[49] K. C. Wong, S. H. Suyu, G. C. F. Chen et al., H0LiCOW XIII. A 2.4% measurement of  $H_0$  from lensed quasars: 5.3 $\sigma$  tension between early and late-Universe probes, *Mon. Not. R. Astron. Soc.* 498, 1420 (2020).

[50] S. Birrer, A. J. Shajib, A. Galan et al., TDCOSMO IV: Hierarchical time-delay cosmography—joint inference of the Hubble constant and galaxy density profiles, *Astron. Astrophys.* 643, A165 (2020).

[51] C. Heymans, T. Tröster, M. Asgari et al., KiDS-1000 Cosmology: Multi-probe weak gravitational lensing and spectroscopic galaxy clustering constraints, *Astron. Astrophys.* 646, A140 (2021).

[52] T. M. C. Abbott, M. Aguena, A. Alarcon et al., Dark Energy Survey Year 3 results: Cosmological constraints from galaxy clustering and weak lensing, *Phys. Rev. D* 105, 023520 (2022).

[53] S. Bocquet, J. P. Dietrich, T. Schrabback et al., Cluster cosmology constraints from the 2500 deg $^2$  SPT-SZ survey: Inclusion of weak gravitational lensing data from Magellan and the Hubble space telescope, *Astrophys. J.* 878, 55 (2019).

[54] T. M. C. Abbott, M. Aguena, A. Alarcon et al., Joint analysis of DES Year 3 data and CMB lensing from SPT and Planck III: Combined cosmological constraints, *Phys. Rev. D* 107, 023531 (2023).

[55] G. Hinshaw, D. Larson, E. Komatsu et al., Nine-year Wilkinson Microwave anisotropy probe (WMAP) observations: Cosmological parameter results, *Astrophys. J. Suppl. Ser.* 208, 19 (2013).

[56] U. Seljak, Gravitational lensing effect on cosmic microwave background anisotropies: A power spectrum approach, *Astrophys. J.* 463, 1 (1996).

[57] A. Lewis and A. Challinor, Weak gravitational lensing of the CMB, *Phys. Rep.* 429, 1 (2006).

[58] E. Calabrese, A. Slosar, A. Melchiorri, G. F. Smoot, and O. Zahn, Cosmic microwave weak lensing data as a test for the dark universe, *Phys. Rev. D* 77, 123531 (2008).

[59] P. Motloch and W. Hu, Lensing covariance on cut sky and SPT-Planck lensing tensions, *Phys. Rev. D* 99, 023506 (2019).

[60] J. Froustey, C. Pitrou, and M. C. Volpe, Neutrino decoupling including flavour oscillations and primordial nucleosynthesis, *J. Cosmol. Astropart. Phys.* 12 (2020) 015.

[61] J. J. Bennett, G. Buldgen, P. F. de Salas, M. Drewes, S. Gariazzo, S. Pastor, and Y. Y. Y. Wong, Towards a precision calculation of  $N_{\text{eff}}$  in the Standard Model II: Neutrino decoupling in the presence of flavour oscillations and finite-temperature QED, *J. Cosmol. Astropart. Phys.* 04 (2021) 073.

[62] C. Brust, D. E. Kaplan, and M. T. Walters, New light species and the CMB, *J. High Energy Phys.* 12 (2013) 058.

[63] P. A. Zyla, R. M. Barnett et al. (Particle Data Group), Review of particle physics, *Prog. Theor. Exp. Phys.* 2020, 083C01 (2020).

[64] K. N. Abazajian, P. Adshead, Z. Ahmed et al., CMB-S4 science book first edition, [arXiv:1610.02743](https://arxiv.org/abs/1610.02743).

[65] R. H. Cyburt, B. D. Fields, K. A. Olive, and T.-H. Yeh, Big bang nucleosynthesis: Present status, *Rev. Mod. Phys.* 88, 015004 (2016).

[66] K. Jedamzik and T. Abel, Small-scale primordial magnetic fields and anisotropies in the cosmic microwave background radiation, *J. Cosmol. Astropart. Phys.* **10** (2013) 050.

[67] K. Jedamzik and A. Saveliev, Stringent Limit on Primordial Magnetic Fields from the Cosmic Microwave Background Radiation, *Phys. Rev. Lett.* **123**, 021301 (2019).

[68] K. Jedamzik and L. Pogosian, Relieving the Hubble Tension with Primordial Magnetic Fields, *Phys. Rev. Lett.* **125**, 181302 (2020).

[69] K. Abazajian, G. Addison, P. Adshead, Z. Ahmed, S. W. Allen, D. Alonso, M. Alvarez, A. Anderson, K. S. Arnold, C. Baccigalupi et al. (CMB-S4 Collaboration), CMB-S4 science case, reference design, and project plan, *arXiv: 1907.04473*.

[70] <http://cc.in2p3.fr>.

[71] R. Pordes et al., The open science grid, *J. Phys. Conf. Ser.* **78**, 012057 (2007).

[72] I. Sfiligoi, D. C. Bradley, B. Holzman, P. Mhashilkar, S. Padhi, and F. Wurthwein, The pilot way to grid resources using glideinWMS, WRI World Congress on Computer Science and Information Engineering Vol. 2 (Institute of Electrical and Electronics Engineers (IEEE), 2009), pp. 428–432.

[73] K. M. Górski, E. Hivon, A. J. Banday, B. D. Wandelt, F. K. Hansen, M. Reinecke, and M. Bartelmann, HEALPix: A framework for high-resolution discretization and fast analysis of data distributed on the sphere, *Astrophys. J.* **622**, 759 (2005).

[74] A. Zonca, L. P. Singer, D. Lenz, M. Reinecke, C. Rosset, E. Hivon, and K. M. Gorski, HEALPy: Equal area pixelization and spherical harmonics transforms for data on the sphere in Python, *J. Open Source Software* **4**, 298 (2019).

[75] J. D. Hunter, Matplotlib: A 2D graphics environment, *Comput. Sci. Eng.* **9**, 90 (2007).

[76] E. Jones, T. Oliphant, P. Peterson et al., Open source scientific tools for Python (2001), <http://www.scipy.org/>.

[77] S. van der Walt, S. Colbert, and G. Varoquaux, The NumPy array: A structure for efficient numerical computation, *Comput. Sci. Eng.* **13**, 22 (2011).

[78] A. P. Lane, Submillimeter transmission at south pole, in *Astrophysics from Antarctica*, ASP Conference Series Vol. 141, edited by G. Novak and R. H. Landsberg (ASP, San Francisco, 1998), p. 289.

[79] J. R. Pardo, J. Cernicharo, and E. Serabyn, Atmospheric transmission at microwaves (ATM): An improved model for millimeter/submillimeter applications, *IEEE Trans. Antennas Propag.* **49**, 1683 (2001).

[80] N. Aghanim, Y. Akrami et al. (Planck Collaboration), Planck 2018 results III. High Frequency Instrument data processing and frequency maps, *Astron. Astrophys.* **641**, A3 (2020).